CHAPTER 5 RESULTS AND DISCUSSIONS

This chapter presents and explains all the experimental results with the corresponding discussions.

5.1 Materials characterization

5.1.1 Bed material

The characterizations of quartz sand provided the important physical and chemical properties.

1. Chemical composition and crystalline structure

The detailed characteristics the chemical composition and crystalline structure of quartz sand were given in Table 5.1 and Figure 5.1.

Table 5.1 Quartz sand properties

Item	
Particle density (kg/m^3)	2,510
Bulk density (kg/m^3)	1,851
Fixed bed void fraction	0.351
Elemental composition (wt%)	
SiO_2	99.55
MgO	0.008
CaO	0.02
Al_2O_3	0.16
Fe_2O_3	0.05
Other	0.212

The chemical compositions, analyzed by XRF, which were reported as the oxide form in Table 5.1 revealed that this sand is almost pure of Si. The XRD spectrum illustrated in Figure 5.1 showed that the peak positions of this sand were perfectly matched with the standard material. This bed material was assertive SiO_2 compound in Hexagonal crystalline structure of quartz. Generally, the amplitudes of peaks in the XRD pattern are directly related to the atomic distances [174].

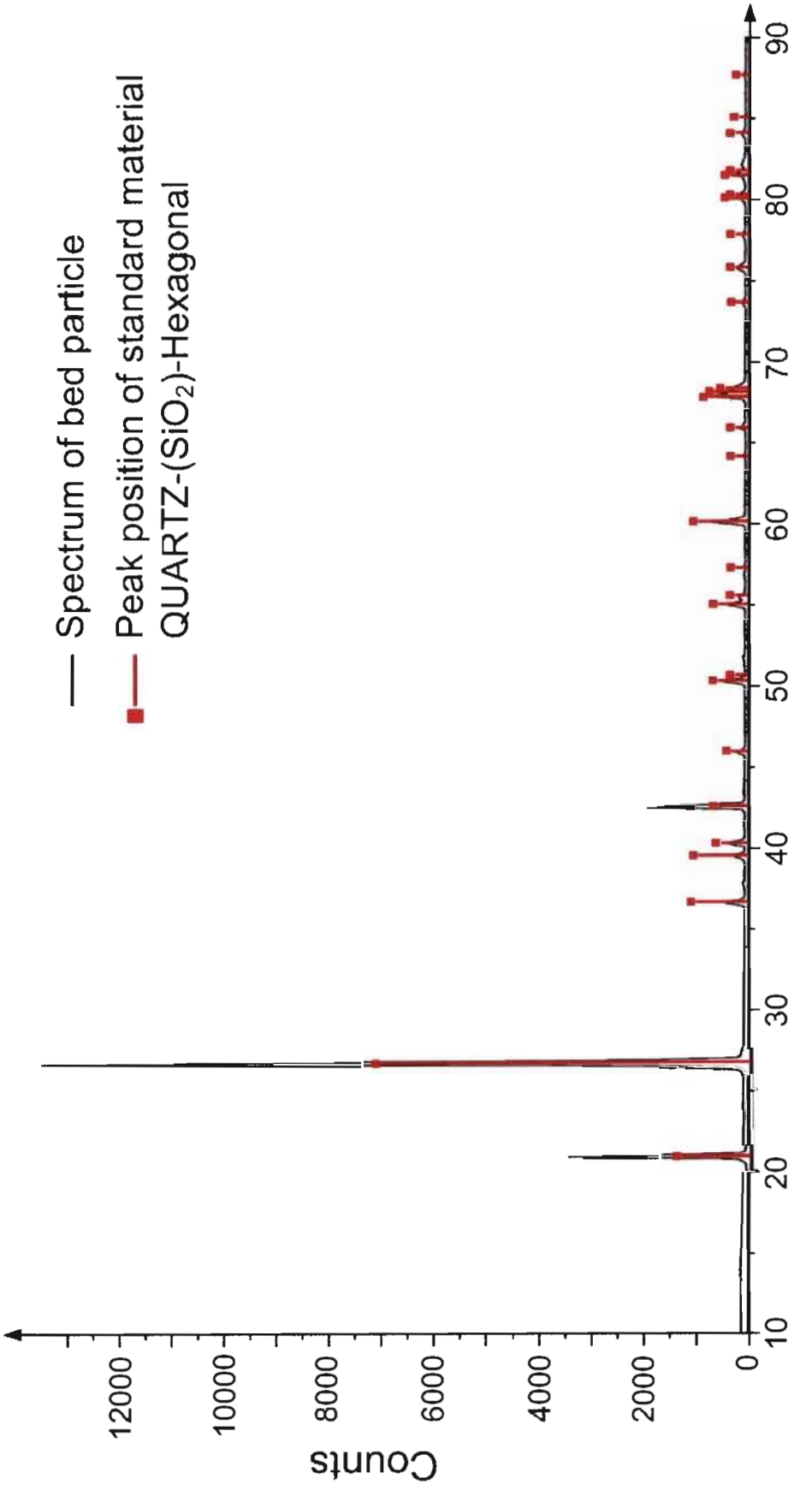

Figure 5.1 XRD analysis of quartz sand particles.

2. Size distribution

The screen analyses of quartz sand used specifically in the present experimental conditions were reported in Figure 5.2.

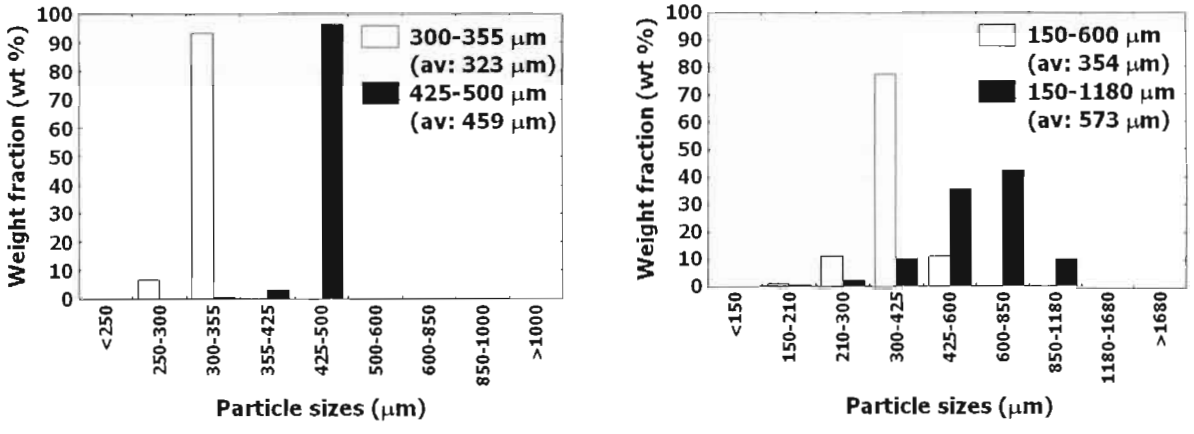

Figure 5.2 Size distributions of fresh sand particle for (a) lab scale and (b) pilot scale experiments.

Since the lab scale agglomeration test was to be the controlled condition, the adopted sizes ranges of sand were intentionally fixed in the relatively narrow distribution (Fig. 5.2a). The size ranges of 300-355 μm (average size, $d_{p,av}$:323 μm) and 425-500 μm (459 μm) were used for lab scale experiments, while those of 150-600 μm (354 μm) and 150-1180 μm (573 μm) (Fig. 5.2b) were used in pilot scale experiments. The diminutive fractions of undesirable size ranges for lab scale tests, however, were still found in bed samples, due to an imperfect separation and cracking.

5.1.2 Biomass

The properties of selected biomass samples were intensively characterized as shown below.

1. Biomass characteristics

The physical, chemical and combustion properties of biomass samples were reported in Table 5.2. They were analyzed based on "as fired basis" and "dry basis".

Table 5.2 Biomass properties

Description	Palm shell	Corncob	Palm bunch	Rice straw
Physical property				
Bulk density (Kg/m^3) [b]	500.04	124.06	28.69	42.56
Chemical property				
Proximate analysis (wt%) [b]				
Moisture	(17.36 [a]) 9.79	10.37	(63.44 [a]) 9.23	10.09
Volatile matter	68.35	72.01	74.48	69.49
Fixed carbon [d]	19.28	16.13	19.29	16.38
Ash	2.58	1.48	6.22	14.13
Ultimate analysis (wt%) [c]				
C	49.30	44.86	34.71	28.62
H	5.88	6.30	4.47	3.76
O [d]	41.52	46.39	53.79	52.49
N	0.40	0.66	0.64	0.89
S	0.019	0.049	0.05	0.09
Cl	0.02	0.06	0.16	0.02
HHV (kJ/kg) [c]	19,030	17,600	17,530	15,215

[a] As received basis; [b] As fired basis; [c] As dry basis; and [d] by subtraction.

Palm shell, the hard and dense shell of palm seed, had relatively high bulk density while corncob, which is the porous cylindrical stalk, showed lower. In contrary, palm bunch and rice straw, both were the fibrous matter, had relatively low bulk density. Due to steaming, palm shell and bunch had considerably high water concentration. Rice straw was a relatively high ash biomass. Sulfur content in these biomass differed only slightly while chlorine content in palm bunch was relatively high, 8 times higher than that of palm shell and rice straw.

2. Ash characteristics

The elements in biomass ash, presented as the oxide form, were reported in Table 5.3. It revealed that silicon proved evidently to be the dominant and abundant element in these ashes. Potassium and magnesium were the major alkali and alkali earth elements presented, respectively. The relatively high content of phosphorus and potassium could be noticed in corncob. From these information, the fluidization during combustion was expected to be problematic in some extent from the influences of the high potassium and chlorine content in these representative biomass fuels.

Table 5.3 Biomass ash compositions (wt% in ash)

Element	Palm shell	Corncob	Palm bunch	Rice straw
SiO_2	61.48	36.60	51.80	60.10
Al_2O_3	2.39	0.56	0.47	0.0
CaO	2.51	0.91	0.95	0.80
MgO	12.95	9.23	18.06	21.97
Na_2O	0.21	0.23	0.33	0.80
K_2O	5.78	33.08	21.39	10.57
P_2O_5	3.96	12.41	4.06	2.45
Fe_2O_3	5.56	5.08	0.72	0.20
Other	5.16	1.9	2.22	3.11

3. Thermal behaviors

The qualitative and quantitative measurement of mass change of the biomass samples associated with thermal degradation was provided by TGA. The amount and rate of change in weight of biomass as a function of temperature in air environment was illustrated in Figure 5.3.

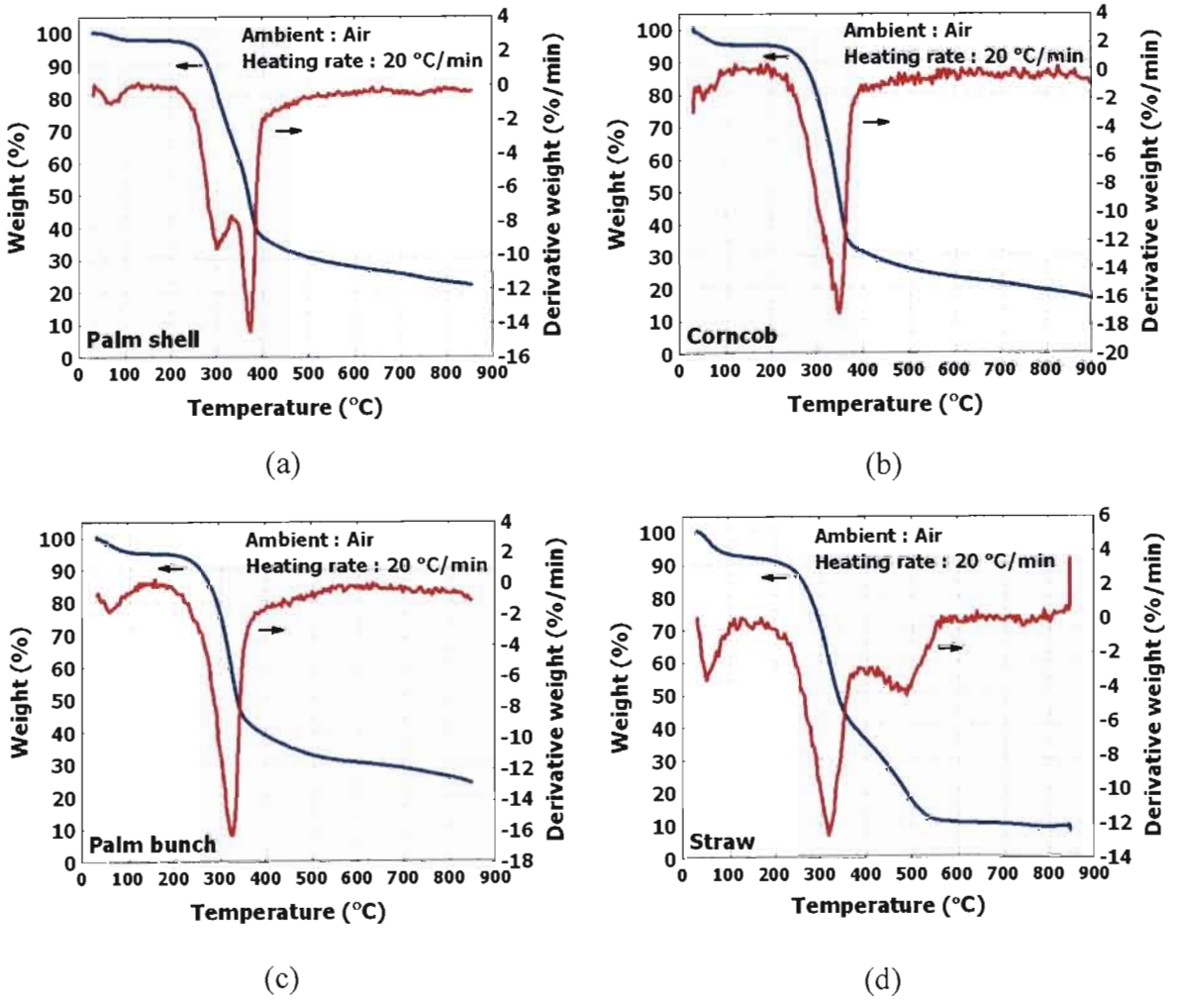

Figure 5.3 TGA weight loss profiles of (a) palm shell, (b) corncob, (c) palm bunch and (d) straw. Noted that all samples were tested based on "as fired basis" in air.

Three distinguishable ranges of the decreasing weight were observed in the relatively similar weight loss profiles. They could be interpreted as the following;

- Moisture in biomass samples began evaporating at about 50 °C until it was depleted at about 100 °C.
- Volatile components then started to release at around 200-230 °C.
- The biomass fuel accessed to the char combustion phase when the temperature reached to about 350-380 °C.

The characteristics of biomass and quartz sand provided the reference data and would be employed in the comparative description with the further results of agglomeration experiments reported below.

5.2 Agglomeration test

The agglomeration tests in both lab and pilot scale fluidized bed combustors were performed under an atmospheric condition and steady state combustion at constant bed temperatures and fluidizing air velocity. The influences of bed temperature (T_b), superficial air velocity (U), bed particle size (d_p), and static bed height (as H_b/D_b) on the bed agglomeration tendency were investigated.

5.2.1 Pre-test

1. Minimum fluidization velocity

The experimental minimum fluidization velocities (U_{mf}) of quartz sand at the given sizes associated to the given temperature ranges of the agglomeration tests were reported in Table 5.4, including the calculated U_{mf} values from Ergan's equation.

Table 5.4 Minimum fluidization velocity data

Size range (μm)	Average size (μm)	Experimental U_{mf} (m/s)	Calculated U_{mf} (m/s)
Lab scale experiment (Temperature range : 750-900 °C)			
300-355	323	0.048-0.051	0.048-0.053
425-500	459	0.078-0.084	0.083-0.091
Pilot scale experiment (Temperature range : 800-900 °C)			
150-600	354	0.055-0.058	0.055-0.060
150-1180	573	0.148-0.152	0.151-0.160

It can be seen that the predicted U_{mf} showed relatively good agreement with the observed values. In this study, 3 to 5 times of these experimental U_{mf} were set as the certain designed experimental conditions to study the air velocity effect.

2. Reference profiles

The bed defluidization which is directly associated to the change in bed hydrodynamics were observed and marked by monitoring the bed pressure and temperature. Therefore, their reference profiles were done before the agglomeration tests by fluidizing the given sand at high temperature without fuel feeding. The typical reference profiles at a specific condition were illustrated in Figure 5.4. It included the typical bed pressure loss and temperature profiles (Fig. 5.4a), and the superficial air velocity (Fig. 5.4b) for 425-500 μm sand size as a function of time in the case of without fuel feeding. Two bed temperatures, T1 and T2, were measured, along the vertical axis, at 2 and 6 cm. height above an air distributor, respectively.

The sand bed early heated up by an electrical heater began to be fluidized at about 600°C. As the temperatures of fluidized bed were increased to about 700 °C, the observed operating parameters began to be logged. The thermal steady state was reached at about 880°C. Adding the cold bed particles into the hot fluidizing bed resulted in a sharp fall about 200°C of bed temperatures, a sudden and double rise in whole bed pressure drop, and a marked increase in amplitude of fluctuation in pressure profiles. The conditions of bed, however, could recover rapidly from this serious disturbance. The isothermal bed temperatures as well as the persistent fluctuation of bed pressure at relatively uniform amplitude and constant baseline were clearly observed in both experimental conditions (H_b/D_b= 0.5 and 1). The changes in amplitude and

baseline of bed pressure relative to the different air velocity were not clearly observed. After 8 hour of trial, no agglomerate was found in the cold spent bed samples.

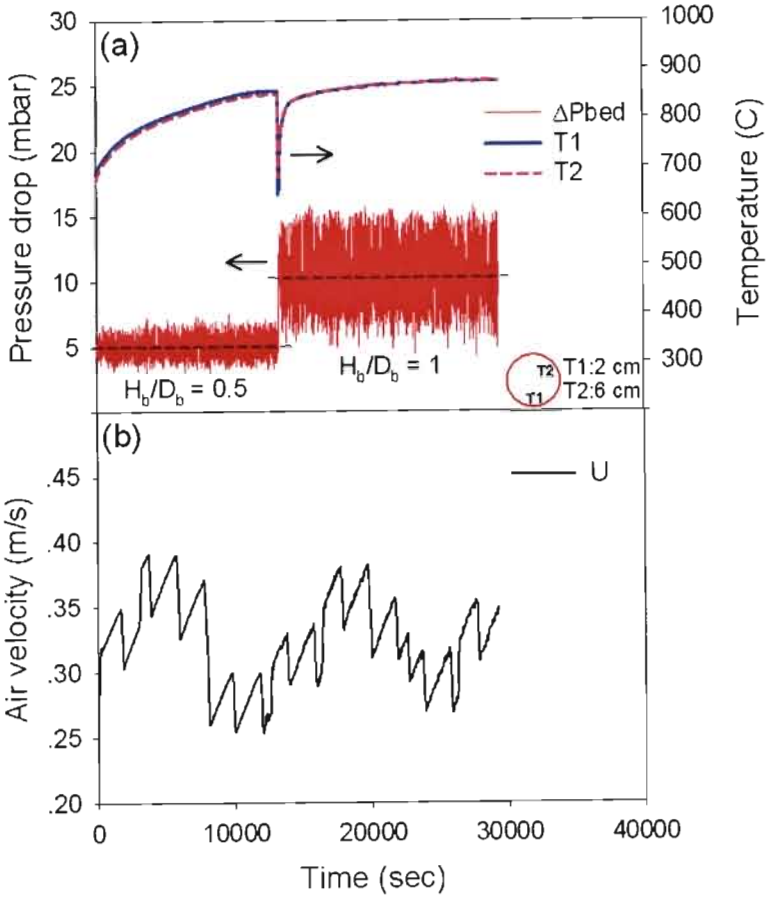

Figure 5.4 Typical bed pressure drop and temperature profiles of the pre-test for d_p=425-500 μm (a) pressure and temperature profile and (b) air velocity.

The isothermal condition inside the fluidized bed was unique due to the intense in-bed heat transfer as a consequence of turbulent bed mixing. Bed pressure drop was directly related to the mass of bed as described by the balance between the net gravitational force and the friction force exerted by fluid in Ergan's equation [148]. The fluctuation in bed pressure originated from the passage of bubbles between the pressure probe and the downwards propagating pressure wave formed by erupting bubbles at the bed surface [148,175]. The increased amplitude as a result of increasing bed height was assumed to be connected to a larger bubble size at the bed surface of higher bed height [175-176], where as an effect of the air velocity on the bed pressure was also in accordance with a previous experimental result [176].

5.2.2 Lab scale agglomeration test

The controlled operating conditions and the main results of lab scale test in term of defluidization time (t_{def}) and potassium consumption to bed mass ratio (K/Bed) were summarized in Table 5.5.

Table 5.5 Summary of operating conditions and main results of lab scale agglomeration test

Run	T_b (°C)	U (m/s)	d_p (μm)	H_b/D_b	K/Bed (x1000)				Defluidization time (t_{def},sec)			
					Palm shell	Corncob	Palm bunch	Straw	Palm shell	Corncob	Palm bunch	Straw
1	700	0.25	300-355	0.5	-	-	1.39	-	-	-	7,061	-
2	800	0.15	300-355	0.5	-	-	0.32	1.16	-	-	1,357	2,326
3	800	0.25	300-355	0.5	-	-	0.43	2.17	-	-	2,262	4,586
4	750	0.15	300-355	1.0	-	-	0.38	1.47	-	-	4,011	5,611
5	800	0.15	300-355	1.0	-	-	0.25	1.02	-	-	2,231	5,201
6	800	0.20	300-355	1.0	-	-	0.28	1.30	-	-	3,286	5,516
7	800	0.25	300-355	1.0	-	-	0.38	2.08	-	-	4,221	6,951
8	850	0.15	300-355	1.0	-	-	0.22	0.88	-	-	1,981	3,516
9	850	0.25	300-355	1.0	2.25	1.39	0.32	1.77	42,353	11,377	2,893	4,473
10	900	0.15	300-355	1.0	-	-	0.20	0.79	-	-	861	2,001
11	800	0.25	425-500	1.0	2.86	1.30	0.28	1.29	55,321	15,793	1,296	3,481
12	850	0.25	425-500	1.0	1.29	0.97	0.24	1.08	26,033	5,793	1,216	2,721
13	900	0.25	425-500	1.0	0.83	0.79	-	-	14,545	5,401	-	-
14	850	0.32	425-500	1.0	2.80	1.10	-	-	42,657	8,681	-	-
15	850	0.40	425-500	1.0	3.53	1.33	-	-	54,281	10,461	-	-
16	900	0.40	425-500	1.0	3.02	1.26	-	-	39,169	8,601	-	-
17	900	0.25	300-355	1.0	2.24	1.10	-	-	26,009	8,553	-	-
18	850	0.25	425-500	0.5	2.22	1.15	-	-	24,081	3,729	-	-
19	850	0.32	425-500	0.5	3.07	1.21	-	-	33,977	4,185	-	-
20	850	0.25	300-355	0.5	3.84	1.51	-	-	40,529	5,425	-	-

1. Bed behaviors

The behaviors of bed during agglomeration were illustrated in Figures 5.5-5.6.

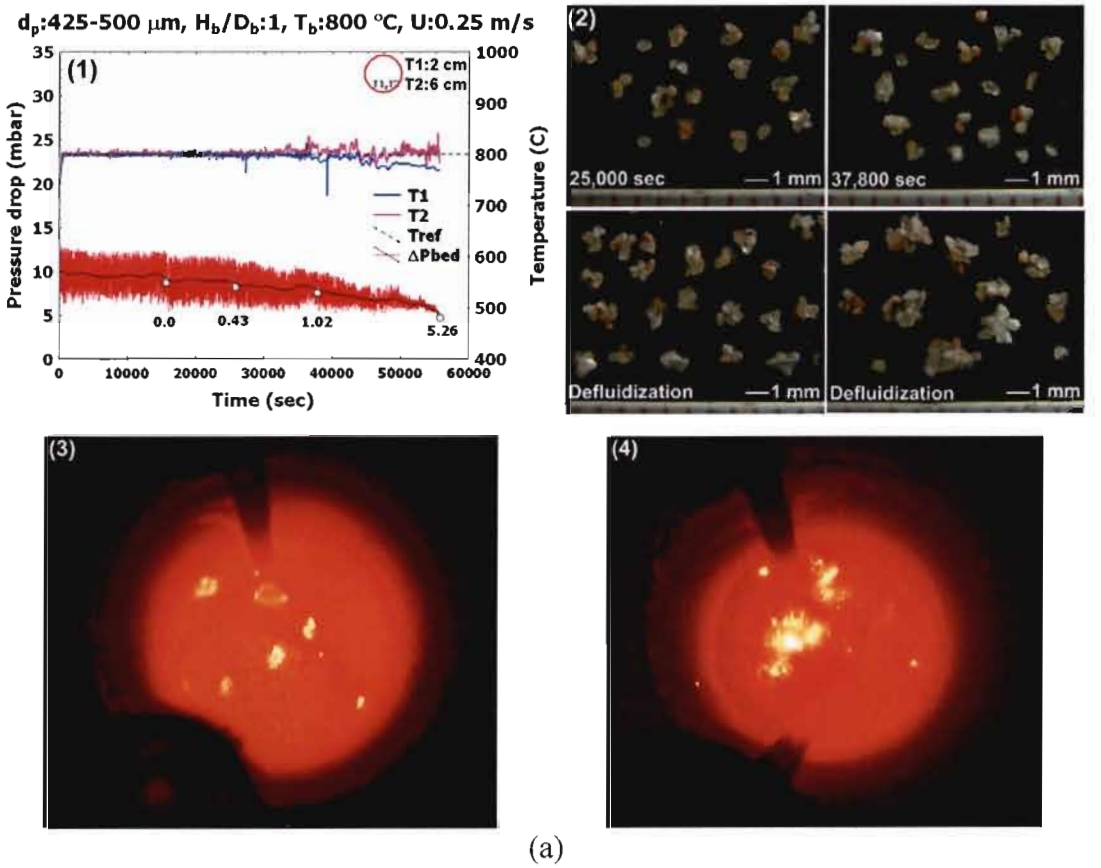

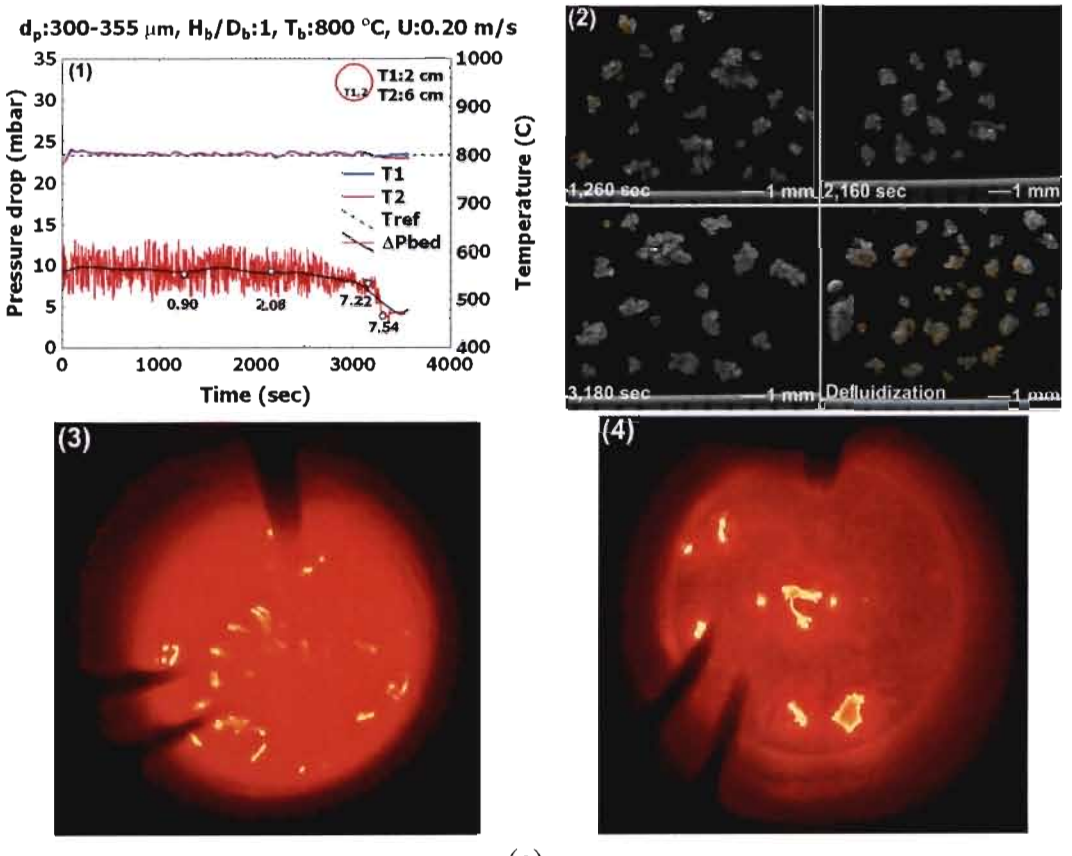

(c)

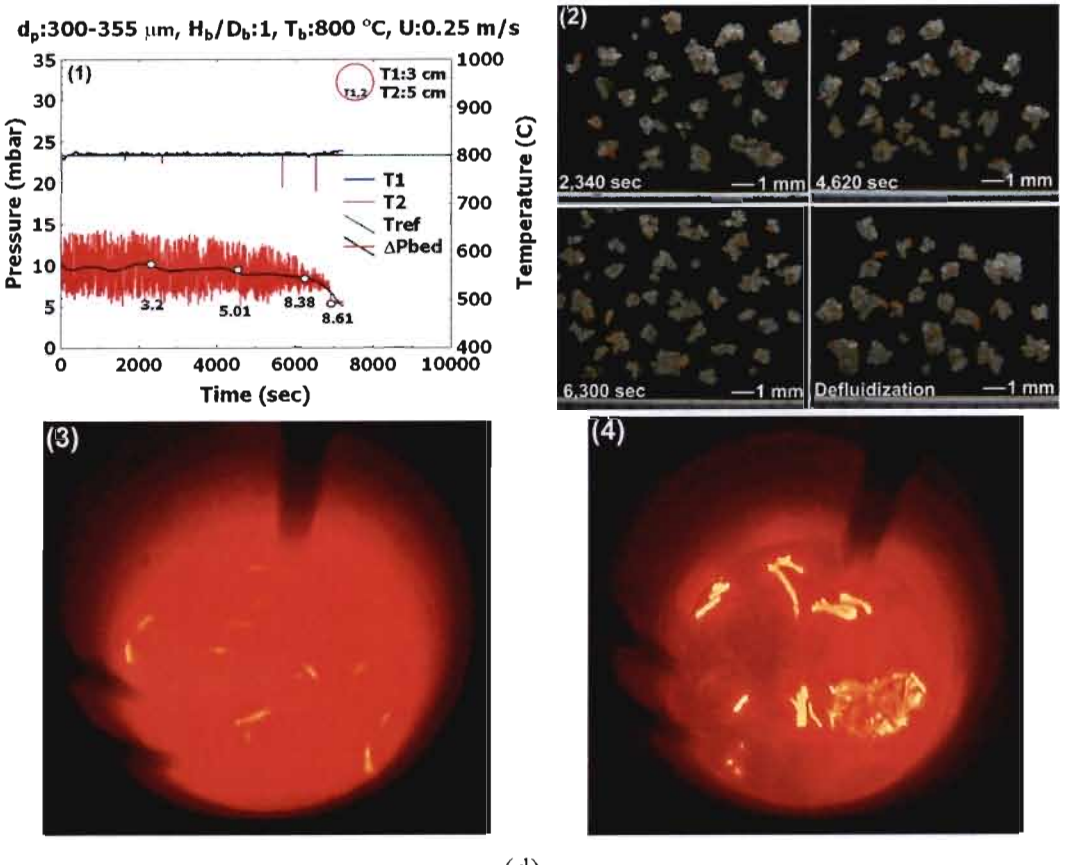

(d)

Figure 5.5 Typical bed behaviors during combustion of (a) palm shell, (b) corncob, (c) palm bunch, and (d) rice straw in lab scale fluidized bed combustor.

The behaviors of bed, as well as the agglomerate samples, at specific conditions during combustion of biomass in a lab scale fluidized bed from start until defluidization were reported typically in Figure 5.5. All biomass samples showed similar behaviors that bed pressure base line and its magnitude of fluctuation upon defluidization decreased steadily during combustion until complete defluidization (Sub-fig. 1), while the non-uniform bed temperatures occurred but it was not clearly observed in a number of trials. The agglomerates accumulated in the bed as the trials progressed. This was indicated by the exponentially increasing percentages of agglomerates in the drawn bed samples at different lengths of operating time, as reported beneath the pressure line. However, the agglomerate fractions were lesser than 10 wt% in all bed samples at complete defluidization. Agglomerates found were formed in various sizes and easily breakable (Sub-fig. 2). Channeling flow of air through the bed at defluidization (Sub-fig. 4), compared with the bed at beginning (Sub-fig. 3), can be observed visually. The higher temperature of fuel particle than bed temperature was noticed by its glowing combustion.

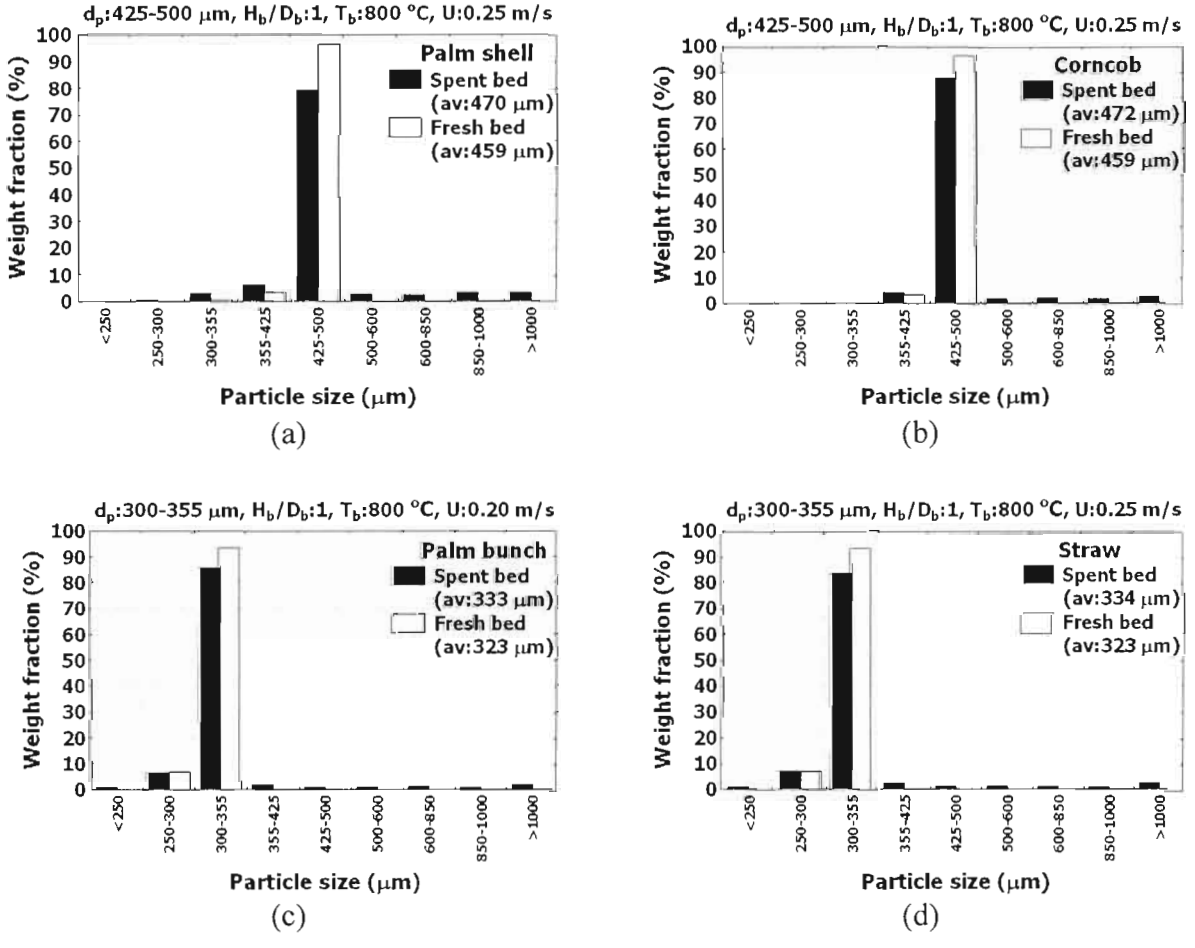

Figure 5.6 Typical particle size distributions of completely defluidized bed compared with fresh bed at specific conditions when burning (a) palm shell, (b) corncob, (c) palm bunch, and (d) rice straw in a lab scale fluidized bed.

An increase in bed particle size was evident from the size analyses of spent bed against fresh bed as shown in Figure 5.6, even though it was affected by partial breaking of agglomerates during discharge and sieving.

An increase in the number and growth of agglomerates inside the bed had established the more multi-size particles in bed. This essentially induced (i) an increased bed void fraction; channeling and decreasing pressure were as a result; the decreasing amplitude was also reflected to the decreasing size of flowing air bubble [176], (ii) a poor bed mixing that caused consequently a segregate combustion zone and local hot spots in bed. The occurrence of bed defluidization that directly affected the bed hydrodynamics was more clearly detectable from the pressure measurement. The bed started to be defluidized as the agglomerates began to be formed, and defluidization was progressively developed from being partial to completion.

To verify the decrease in experimental bed pressure drop, which is caused mainly by the bed agglomeration but can not be affected by the amount of samples taken out for analyses, the bed pressure drop of each trial was therefore estimated by Ergan's equation using initial particle size, and from the retained mass of bed material upon defluidization, and was found to be considerably higher (96-97% of initial bed pressure drop) than that of observed experimental values (60-75% of initial bed pressure drop upon defluidization). This clearly indicated that the decrease of bed pressure drop during the trial is certainly caused by bed agglomeration.

2. Bed agglomeration tendency

The main results of the lab scale agglomeration test in Table 5.5 were reported in terms of the defluidization time (t_{def}) and potassium to bed ratio (K/Bed). t_{def} was the time interval from the start of fuel feeding to the complete defluidization. The defluidization rate, or the formation rate of agglomeration, was inversely proportional to t_{def}; the lower the t_{def}, the higher this rate. K/Bed was well-defined as the maximum of potassium consumed by bed until complete defluidization. It was calculated as the total potassium input from fuel consumption divided by the initial bed inventory, which referred to the quantity of K consumed to completely defluidize the bed. The influences of the bed operating variables on the bed agglomeration tendency were described allegorically by t_{def} and K/Bed. In order to elucidate easily on the bed agglomeration tendency, the results in Table 5.5 were repeated graphically into Figures 5.7-5.11 viz.

It was noticed in Table 5.5 that, entirely, FBC of all given biomass fuels at given operating conditions suffered eventually the defluidization.

- **Effect of fuel inorganic composition**

In Figures 5.7a and 5.7b with the same operating conditions on Run No.9, 11 and 12, the effect of ash composition showed very significant on the bed agglomeration. The outstandingly larger t_{def} and K/Bed of palm shell indicated to its lower bed agglomeration tendency, while palm bunch also showed the markedly opposite results. This could be attributed to the comparatively low K content of palm shell. The higher K content can lead to the larger amount of formed eutectic melts serving as an adhesive material in agglomerates [51]. However, this reason was evidently uncertain. Palm bunch combustion showed the relatively higher tendency in all cases over than corncob combustion, as indicated by lower t_{def} and K/Bed, despite its significantly lower K content (Fig. 5.7c). It might be caused by the relatively high Cl content of palm bunch, which could facilitate the release of inorganic species and enhance the formation of molten K-derived compounds [62,69,85]. The evidences to this effect would be shown and discussed later, elsewhere. The agglomeration tendency of corncob against with rice straw could not be given clearly in comparison.

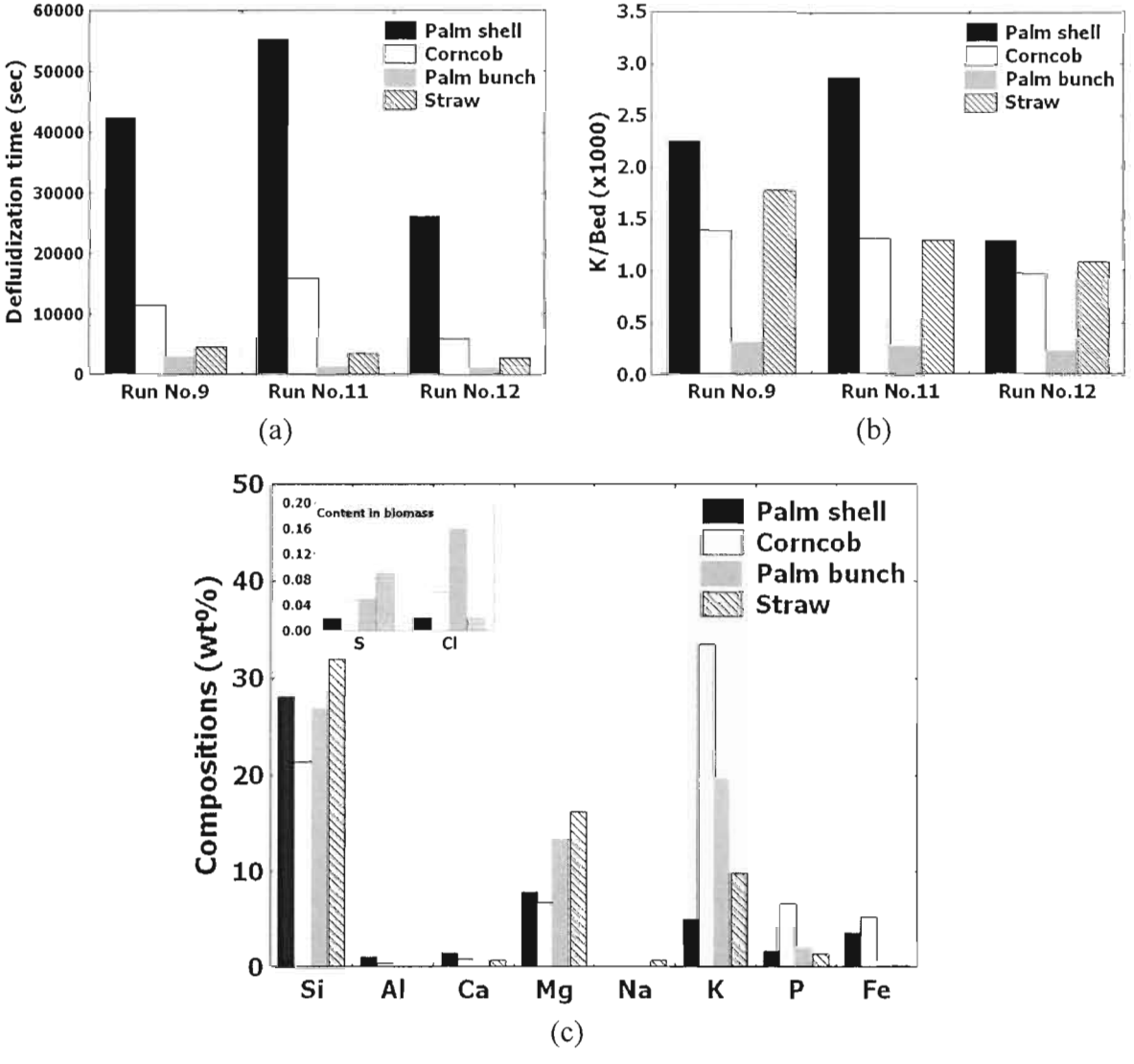

Figure 5.7 Bed agglomeration tendencies on fuel ash compositions described by (a) t_{def} (b) K/Bed, and(c) summary of biomass inorganic content.

- **Effect of bed (combustion) temperature**

t_{def} and K/Bed as a function of bed temperature were illustrated in Figure 5.8 and these results indicated that the bed temperature showed a significant effect. They both decreased exponentially as the bed temperature increased. The lower t_{def} at higher bed temperature came about the lesser K fed into bed, at relatively close fuel feed rate. As the temperature that exceeds the initial melting point of the ash-forming compounds in bed increases, the melt fraction increases [24] and viscosity of the melts decreases resulting to increase the adhesion efficiency [91]. Both factors may result in an increase of the amount and stickiness of coated bed particles by the melt. This in turn accelerates the defluidization process.

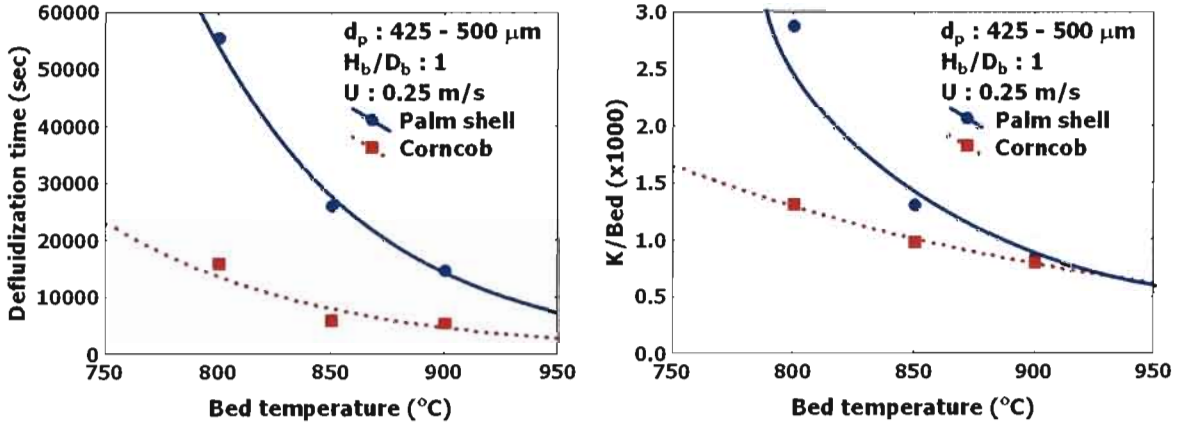

(a)

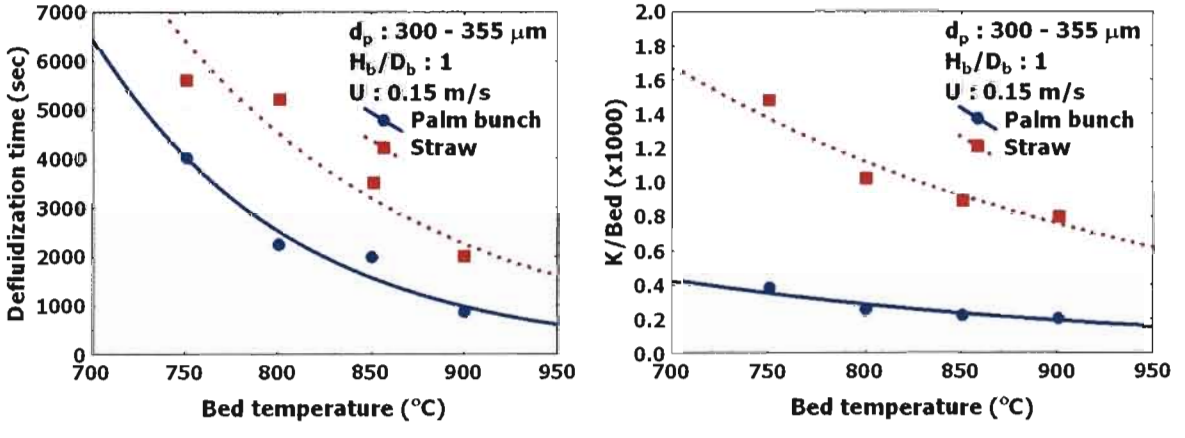

(b)

Figure 5.8 The effects of controlled bed temperature on the bed agglomeration tendency when burning (a) palm shell and corncob, and (b) palm bunch and rice straw in a lab scale fluidized bed.

- **Effect of superficial air velocity**

As shown in Figure 5.9, t_{def} and K/Bed for all biomass increased as the air velocity increased. The higher fluidizing air velocity increases the mobility of bed particles and the resultant force acting on the bed particles, induced by the gas bubbles [147-148]. This causes an increase in the attrition rate of coating, the elutriation rate of fine ash particles and the breaking rate of agglomerates via collision. These phenomena delay the defluidization, and the agglomerates needs more the ash melt to consolidate in order to reach the defluidization state.

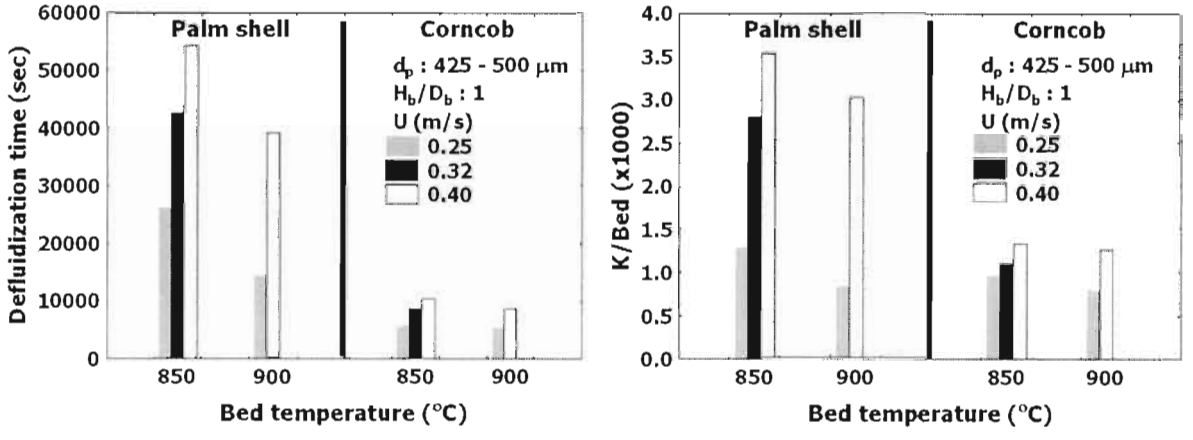

(a)

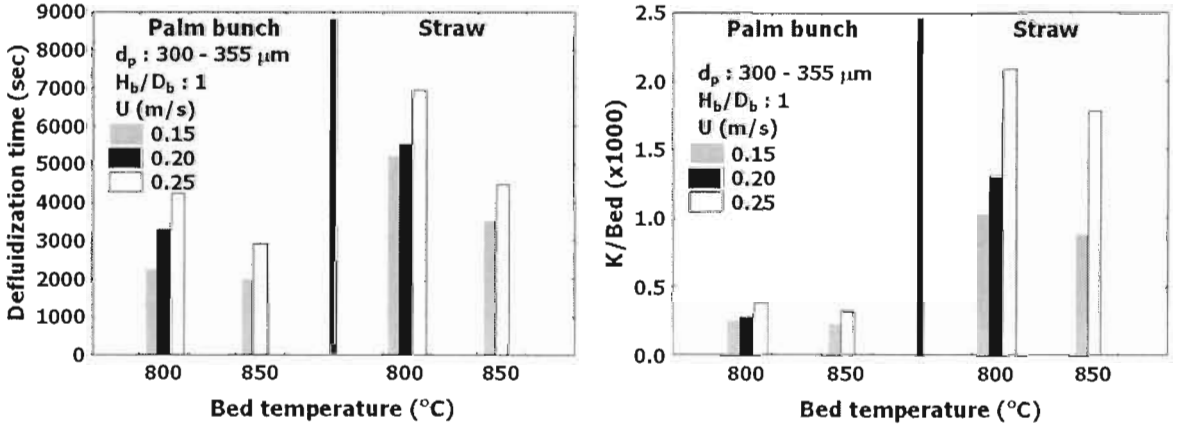

(b)

Figure 5.9 The effects of controlled fluidizing air velocity on the bed agglomeration tendency when burning (a) palm shell and corncob, and (b) palm bunch and rice straw in a lab scale fluidized bed.

- **Effect of bed particle size**

In the set of trials carried out with two different bed particle sizes, it was shown in Figure 5.10 that an increase of bed particle size clearly resulted in the lower t_{def} and K/Bed. A bed with the larger particle size has lower outer specific surface area, so it needs less the ash melts to form coating layers and necks. In additions, the bed mixing of larger bed grain is poorer at the same air velocity as the ratio of U/U_{mf} is lower, due to the higher U_{mf} for larger particles. This feature easily causes hot spots in bed, which enhances the formation of ash melt and the vaporization of ash constituents [51,110]. These two factors facilitate agglomeration and then accelerate defluidization.

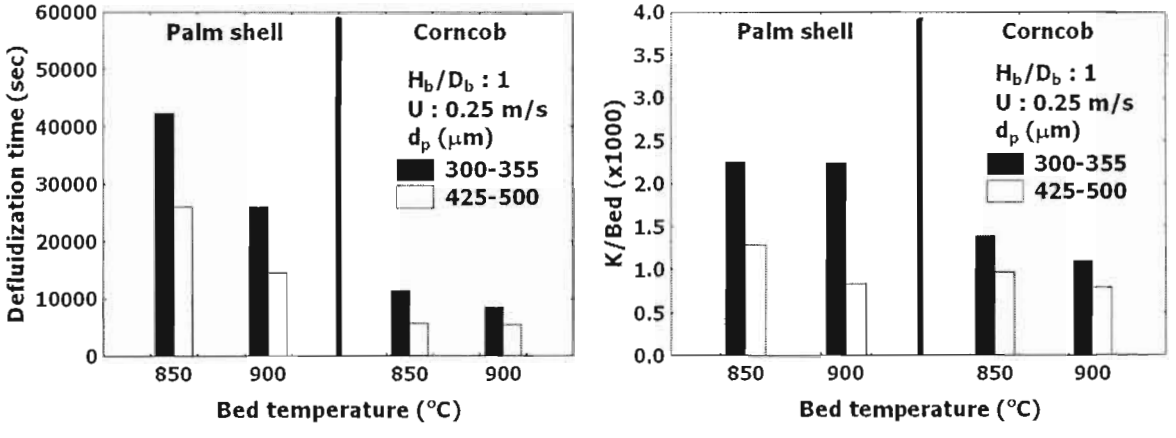

(a)

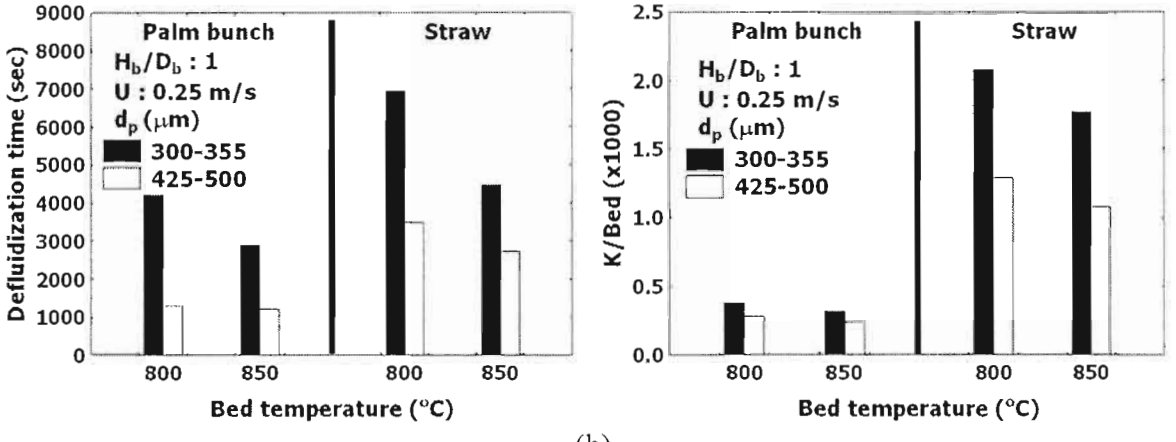

(b)

Figure 5.10 The effects of controlled sand size on the bed agglomeration tendency when burning (a) palm shell and corncob, and (b) palm bunch and rice straw in a lab scale fluidized bed.

In case of the same U/U_{mf} ratio at which the bed mixing behavior is supposed to be similar (Run No. 5 vs. 11 and 8 vs. 12 in Table 5.5), the increase of bed particle size showed the higher K/Bed. It is due to that larger particle has more inertia which consequently related to the higher energetic collision. Therefore, the adhesion to form agglomerates should be more difficult [51] and require the more amount of ash melt to form agglomerate. t_{def} may can not provide well suitable description in bed agglomeration tendency in this case, due to the difference in fuel feed rate as a consequence of the enhanced in-bed heat transfer and heat loss by flue gas from increasing air flow rate.

- **Effect of static bed height**

A set of the results for the effect of static bed height at different biomass was showed in Figure 5.11. The bed height was increased doubly as the mass of bed increased twice accordingly. The biomass consumption relative to K consumption in most trials increased less than twice and K/Bed for higher static bed height is resultantly lower. The increasing static bed height yields more surface area of bed particles, hence needing more amounts of ash melt, while the bed mixing is poorer and the ash melt in smaller fraction can stick easily to particles to form agglomerates. For this reason, the K/Bed of higher H_b/D_b showed lower while t_{def} showed an increasing trend, due to the poorer bed mixing. In this study, the effect of poor bed mixing was clearly seen from the reasonable decrease of K/Bed which otherwise would be relatively constant in value when the static bed height was doubled.

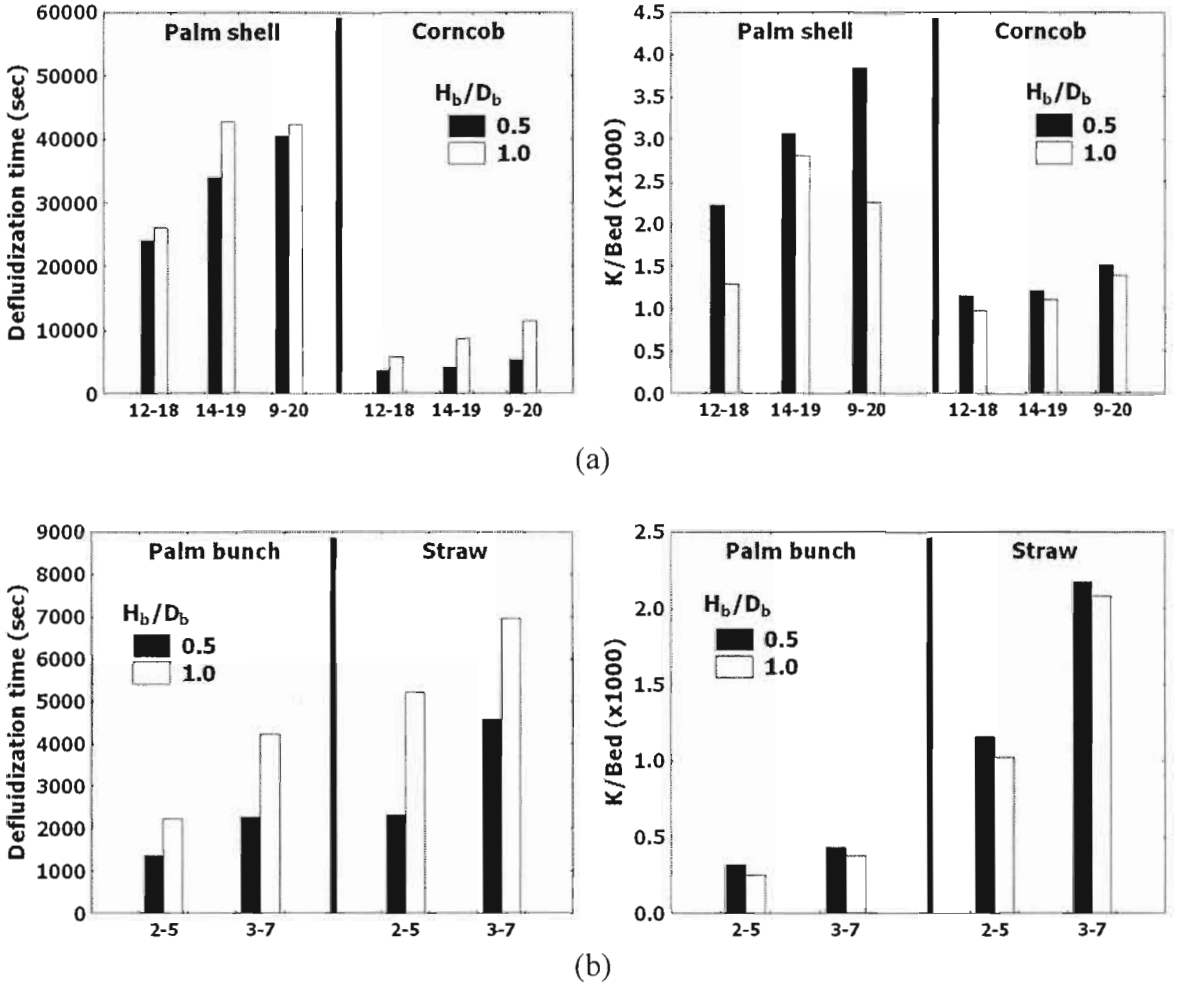

Figure 5.11 The effects of controlled static bed height on the bed agglomeration tendency when burning (a) palm shell and corncob, and (b) palm bunch and rice straw in a lab scale fluidized bed (No. in x-axis represent No. of Run in Table 5.5).

The influences of bed temperature, air velocity, particle size and static bed height on the bed agglomeration tendency in the present work were consistent with the experimental results reported in previous literatures [18,51,108-111,154].

The contributions of operating variables on the tendency of bed agglomeration in present work could be summarized in Table 5.6.

Table 5.6 Present summaries of bed variable contributions

Variable	Tendency
Alkali content	+
Bed temperature	+
Fluidizing gas velocity	-
Bed particle size	+
Static bed height	+

where the defludization by bed agglomeration was accelerated by an increased magnitude of a variable is described by the plus (+) and the opposite trend was referred as the minus (-).

t_{def} and K/Bed in this work showed good consistency and could be well for comparative characterization toward the bed agglomeration tendency. However, it must be noted that the elutriation loss of ash was not taken into account in K/Bed. t_{def} is also relative to the fuel feed rate It had been suggested that the rate of defluidization is considered to be the competition between the formation rate of stable bond and the breaking rate of agglomerated particles [109]. The former is a result of melt formation while the latter is significantly dependent upon the fluidization characteristics. Defluidization can take place rapidly if the former process is enhanced by the accumulation of K in bed and/or the increasing bed temperature; and the latter process is worsened by some certain conditions leading to the poor bed mixing.

5.2.3 Pilot scale agglomeration test

The conditions and results of pilot scale experiment similarly reported in term of t_{def} and K/Bed were shown in Table 5.7.

Table 5.7 Summary of pilot sale results

Run	Biomass	T_b (°C)	U (m/s)	$d_{p,av}$ (μm)	$H_b/D_{b,eq}$	Result	
						K/Bed (x1000)	t_{def} (sec)
1	Corncob	850	0.59	573	0.5	1.12	5,797
2	Palm shell	860	0.59	573	0.5	2.99	14,711
3	Palm shell	900	0.61	573	0.5	2.81	13,426
4	Palm bunch	810	0.35	354	0.5	1.02	2,376
5	Palm bunch	850	0.37	354	0.5	0.63	1,331
6	Rice straw	820	0.35	354	0.5	2.42	4,031

1. Bed behaviors

The behaviors of bed in pilot scale fluidized bed during agglomeration were illustrated in Figures 5.12-5.13.

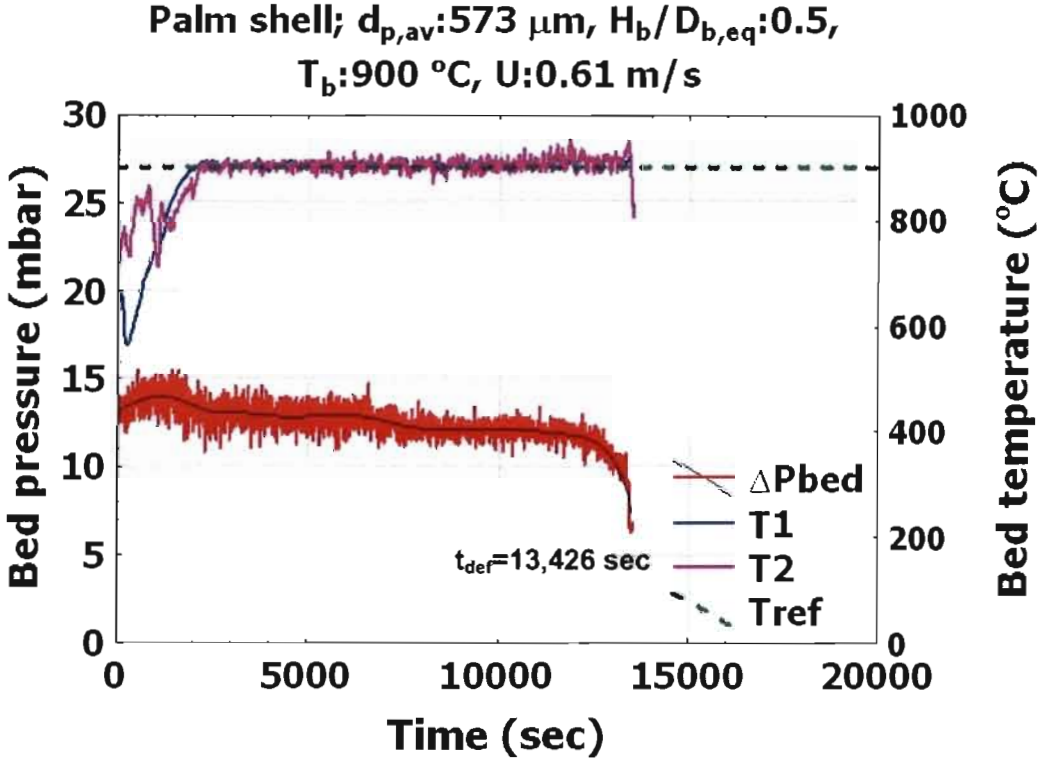

(a)

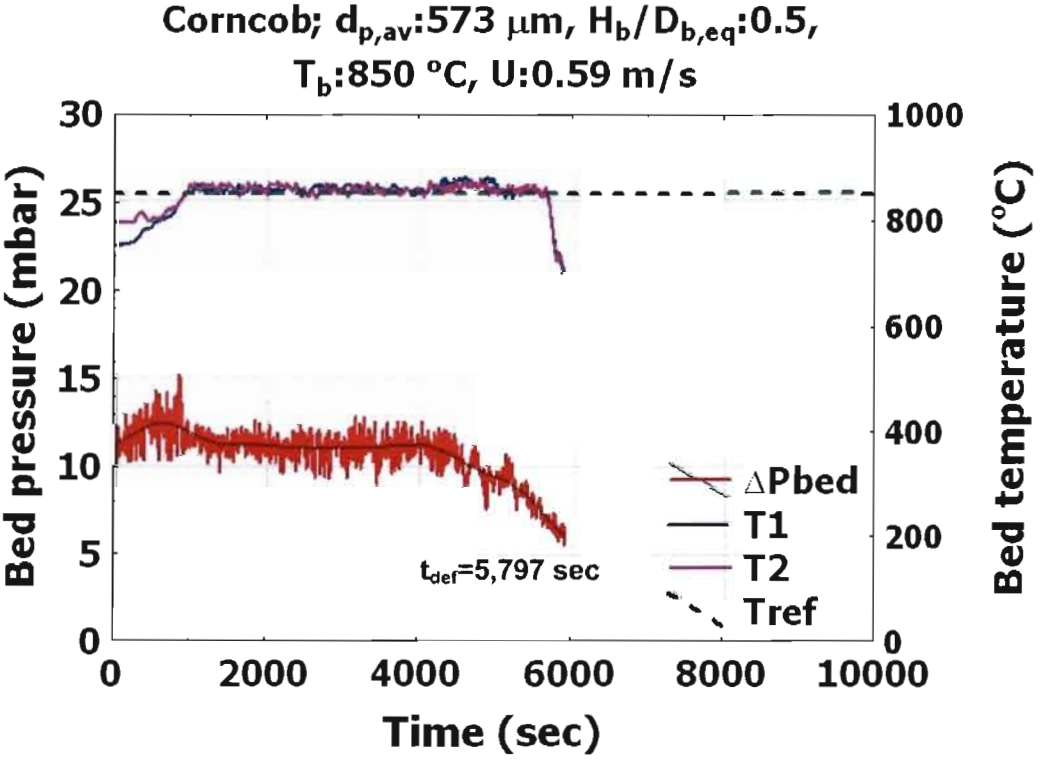

(b)

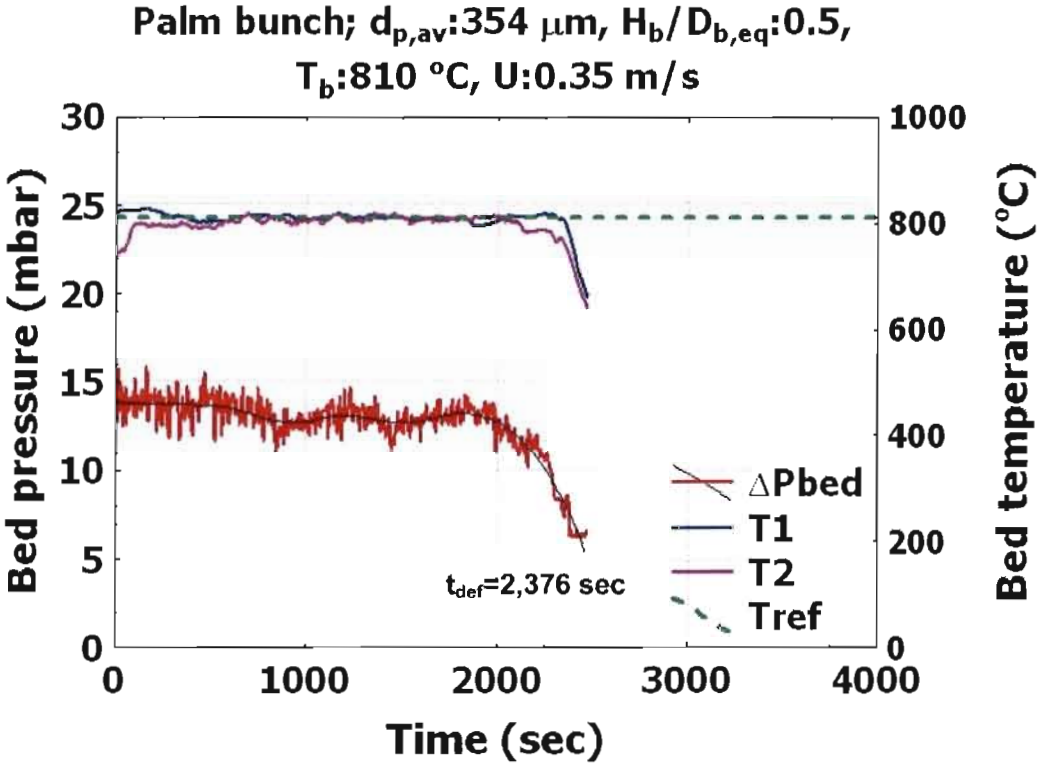

(c)

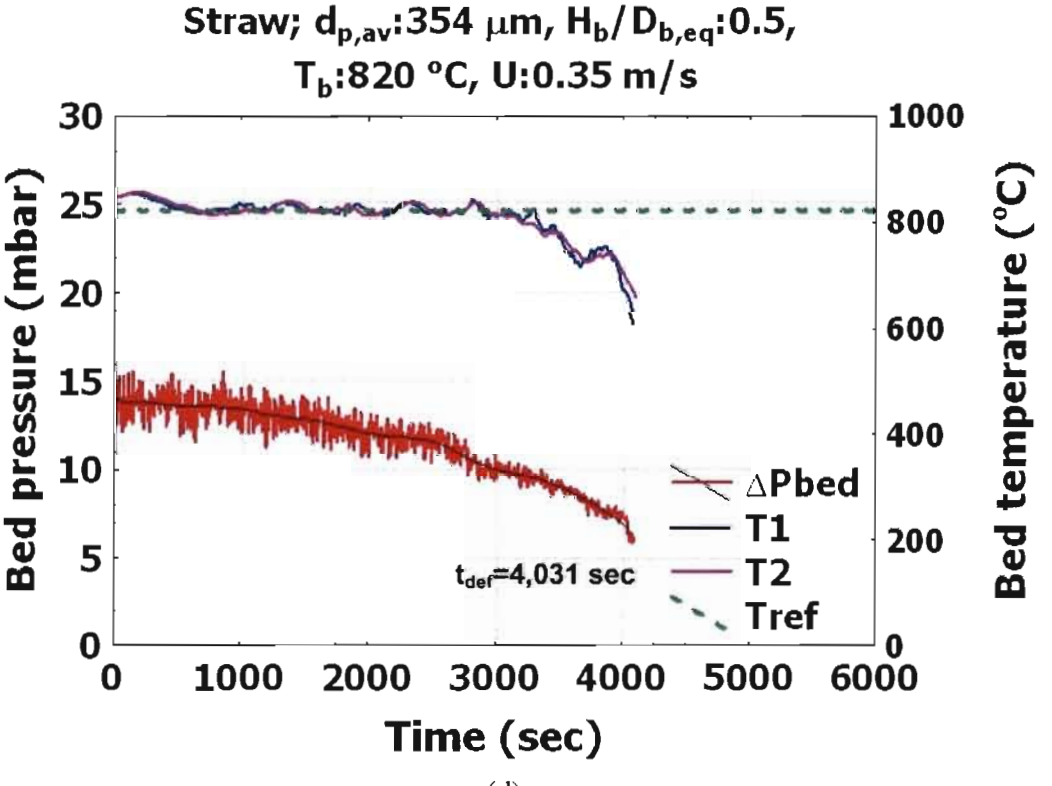

(d)

Figure 5.12 Typical bed pressure loss and bed temperature profiles during agglomeration in a pilot scale fluidized bed burning (a) palm shell, (b) corncob, (c) palm bunch and (d) rice straw.

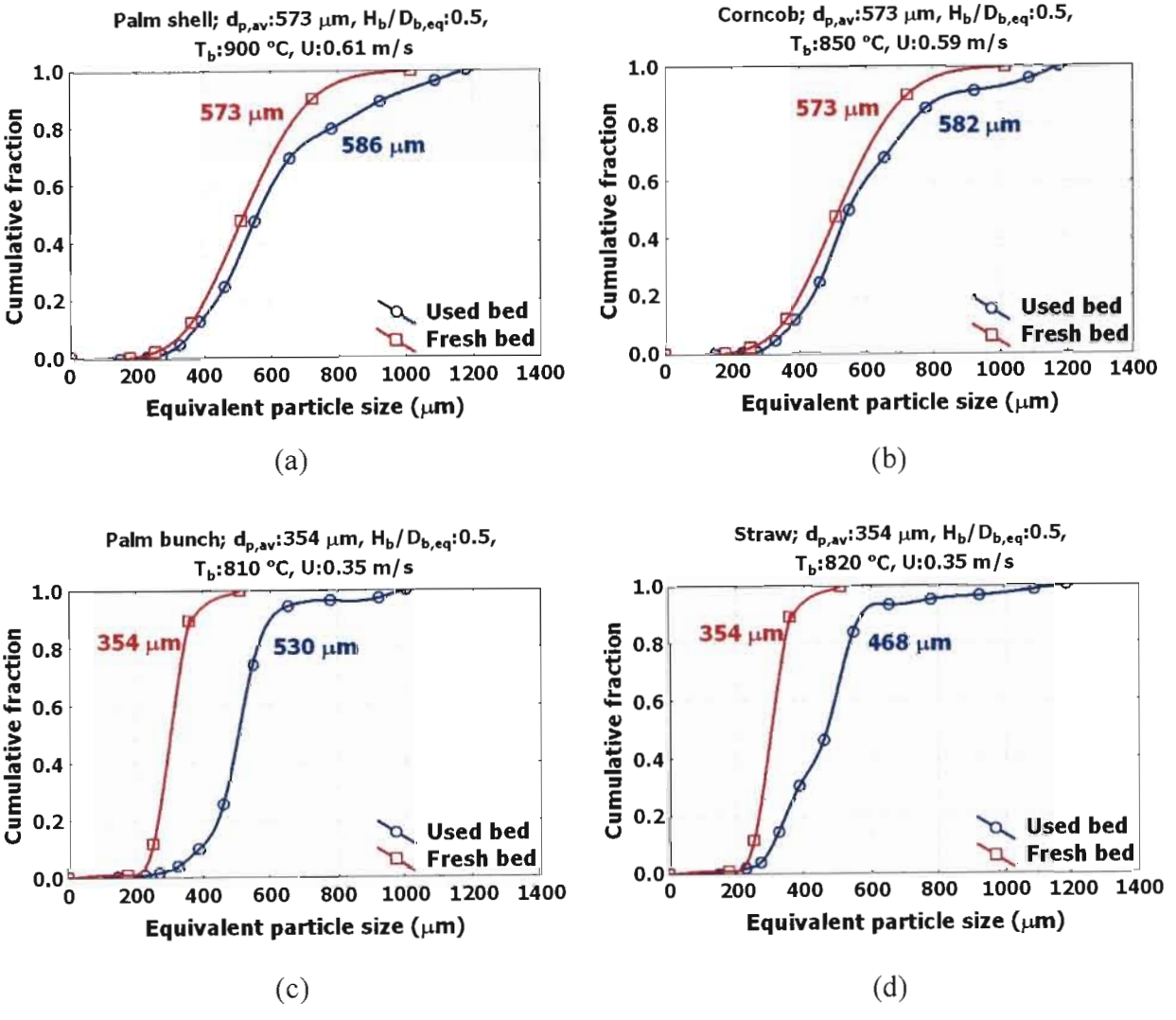

Figure 5.13 Typical size distribution of bed particle in a pilot scale fluidized bed burning (a) palm shell, (b) corncob, (c) palm bunch and (d) rice straw compared with the fresh bed.

The illustrations of typical bed pressure drop and temperature profiles during combustion in pilot scale FBC were shown in Figure 5.12. The similarity in bed behaviors relative to the lab scale test could be observed. As defluidization started, the pressure baseline and magnitude of fluctuation decreased until complete defluidization. Inhomogeneous bed temperatures were clearly observed. After the test, the bed particles had larger mean size, as depicted in Figure 5.13. The extension of bed agglomeration induced the increasing voidage inside bed as indicated by descending bed pressure and the decreasing amplitude, which was connected to the decreasing size of flowing air bubble through the bed. The subsequent result of poor bed mixing occurred and caused the segregated combustion zone in bed, and was shown by the inhomogeneous bed temperatures.

2. Bed agglomeration tendency

As reported in Table 5.7, the comparative degree of bed agglomeration affected by operating parameters also showed an agreement to some results of lab scale test. Corncob and palm bunch showed the higher bed agglomeration tendency than palm shell and rice straw, respectively, as indicated by their entirely lower in t_{def} and K/Bed. The higher content of problematic K and Cl elements is the main reason. The higher combustion temperature can accelerate the defluidization (Run No. 2 vs 3 and 4 vs 5).

5.3 Agglomerate characterizations

In order to investigate the interactions of the ash forming constituents with the bed particles, SEM-EDS analyses were carried out. A set of typical SEM images on the cross-sectioned agglomerates obtained from the bed at defludization state of some conditions were shown below. The EDS spot compositions given in the accompanying multiple bar graphs corresponded to the numbering.

5.3.1 Lab scale agglomerates

Figures 5.14 to 5.17 showed the SEM micrographs in backscatter mode of agglomerate samples at defluidization during combustion of palm shell, corncob, palm bunch, and rice straw, respectively, in lab scale fluidized bed.

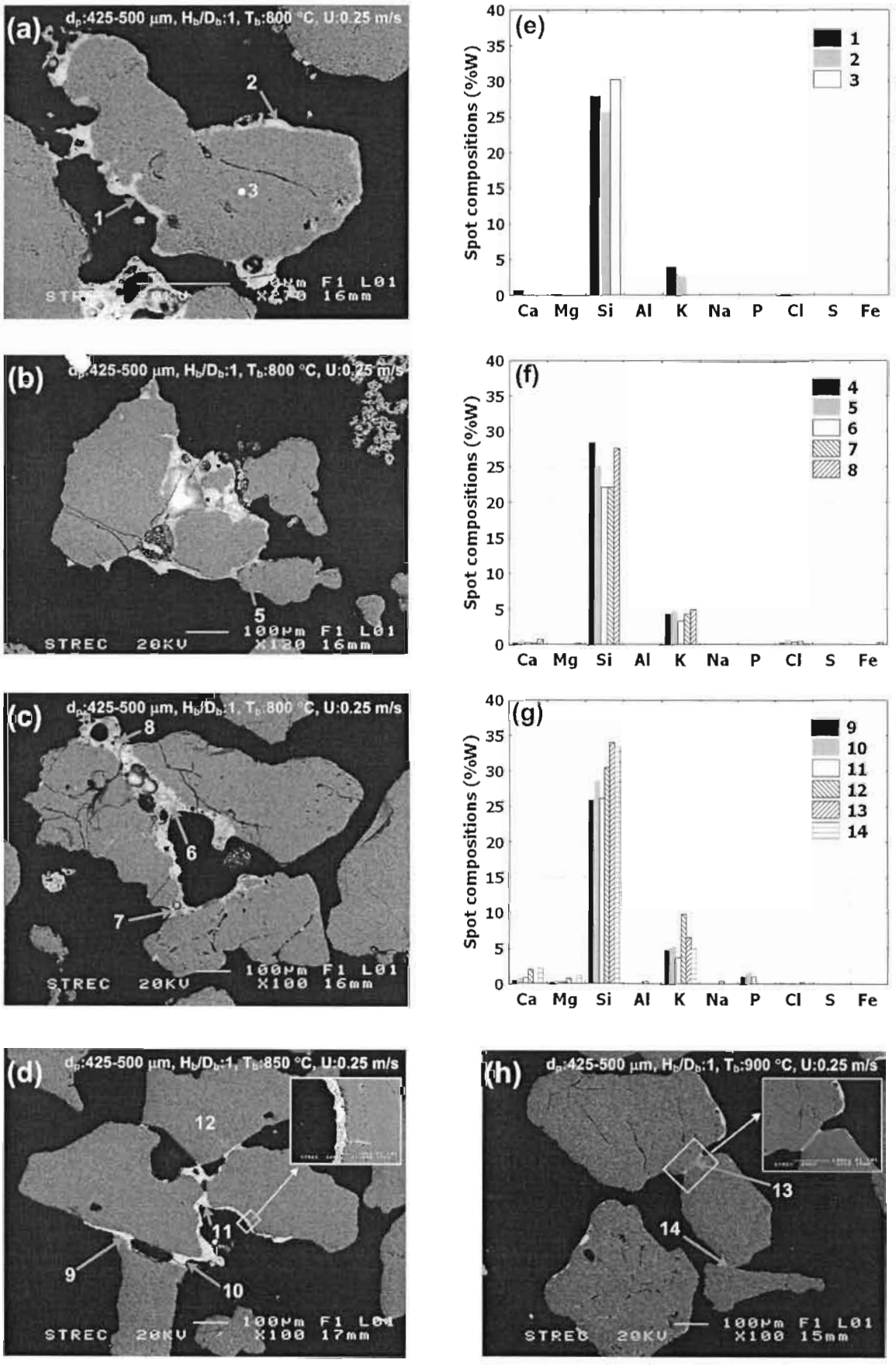

Figure 5.14 Typical SEM images and Spot EDS compositions of palm shell agglomerates from lab scale FBC tests.

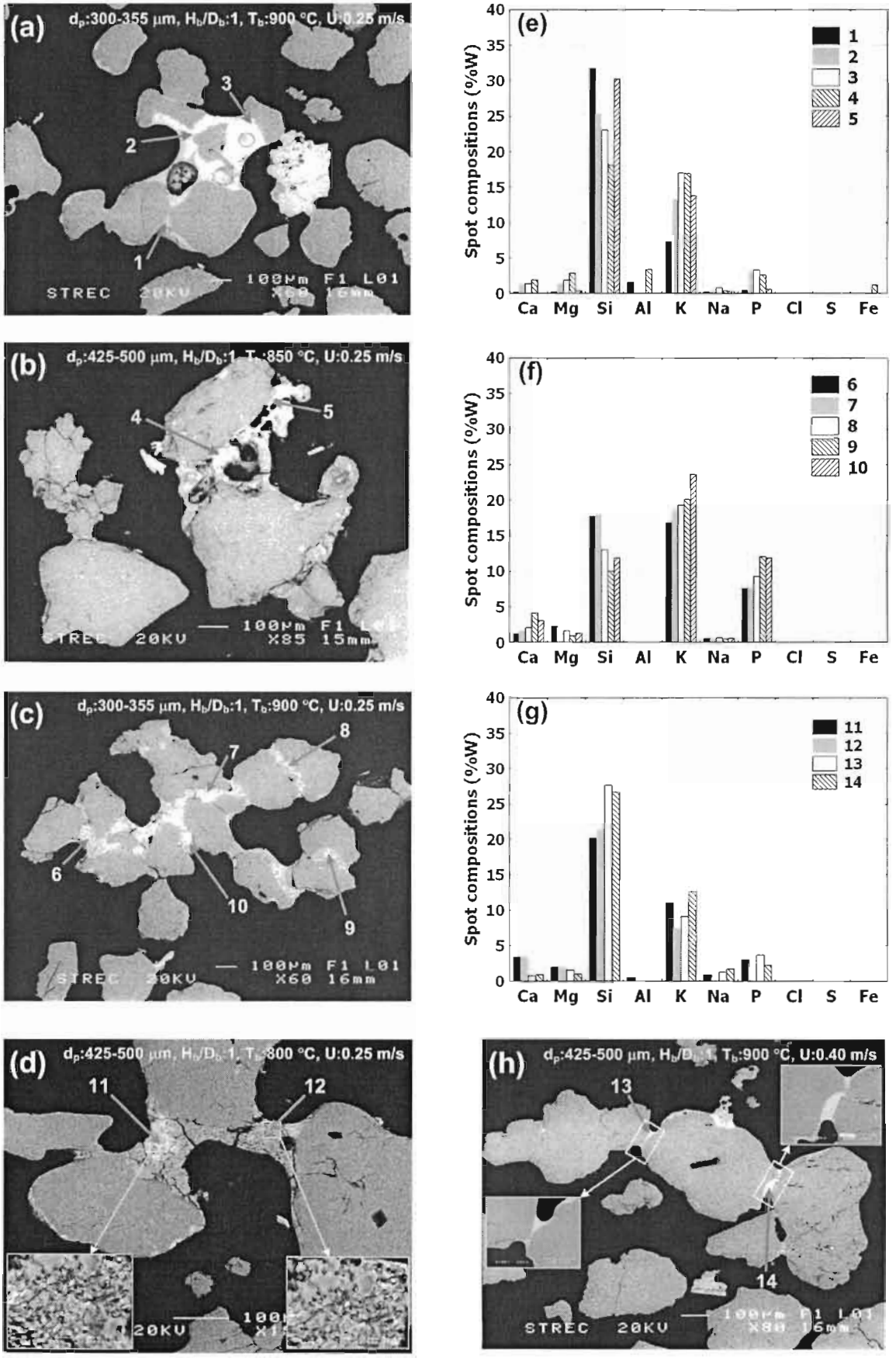

Figure 5.15 Typical SEM images and Spot EDS compositions of corncob agglomerates from lab scale FBC tests.

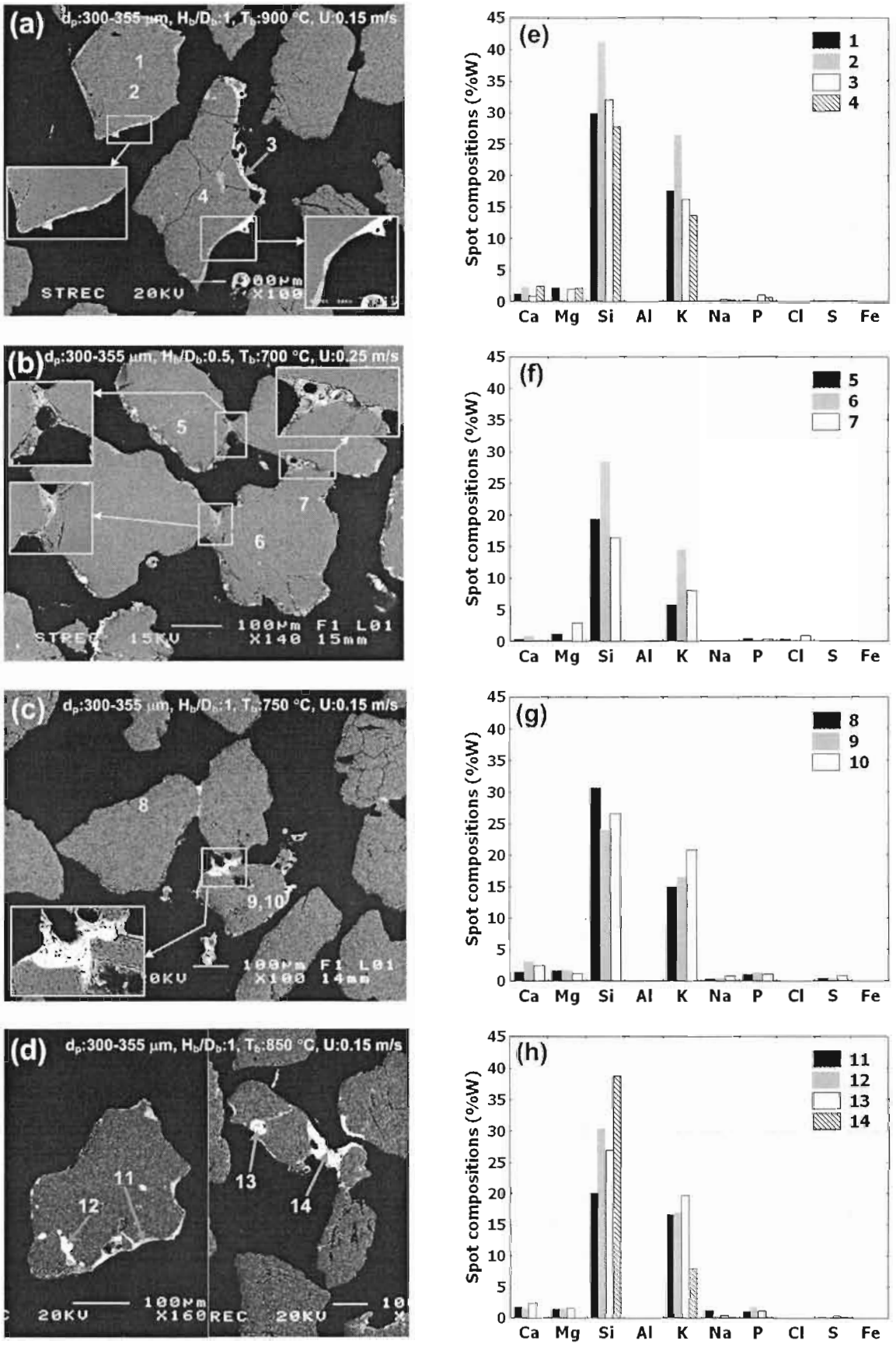

Figure 5.16 Typical SEM images and Spot EDS compositions of palm bunch agglomerates from lab scale FBC tests.

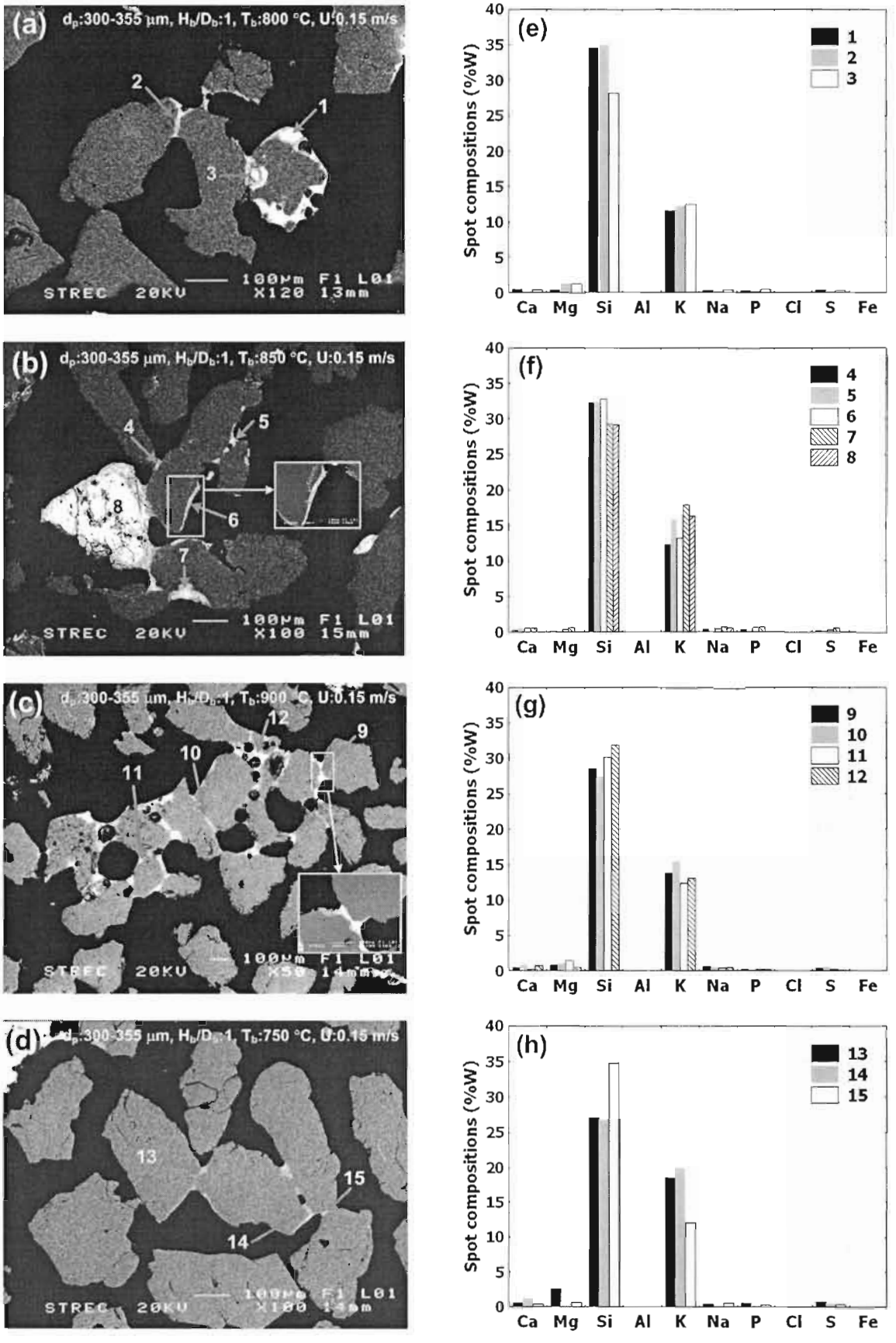

Figure 5.17 Typical SEM images and Spot EDS compositions of rice straw agglomerates from lab scale FBC tests.

In Figures 5.14-5.17, they revealed that sand particles (gray) in agglomerates were covered and cohered together by the fused materials (white) rich in Si and K, and Na, Ca, Mg and P to a lesser extent. Relatively, the rich P in the corncob agglomerates was noticed. S in diminutive fraction was detected while it seemed that Cl vanished in agglomerates.

Sand grains captured in agglomerates were attached together by either neck of material (Fig. 5.14h) or bonded layer (Fig. 5.14c). Both the total (Fig. 5.14b, 5.15a and 5.17a) and partial (Fig. 5.14d and 5.16a) coatings on bed particles could be observed. Concave and convex edges in the features of coating and neck appeared on the polygon shaped sand. The hollow structure had been found on bed particle surfaces (Fig. 5.14a and 5.16a) or located between the sand particles (Fig. 5.14c, 5.15b, 5.16c and 5.17c). The porous coating layers and necks were observed (Figure 5.14d, 5.15d and 5.16a). These non-homogeneous structures were commonly found while thin necks of relatively homogeneous matter were found in a specific contact point between particles (Figure 5.14h, 5.15h and 5.17d). The attack propagating inwards sand grain (in cracks or surface diffusion) was noticed in some palm bunch agglomerates (Fig 5.16d).

The above results gave clear evidence that the formation of biomass ash derived molten compounds, which presented likely as Potassium Silicates, was the main reason for the bed agglomeration in this study. The hollow structures indicated that the burning char particle was previously located inside. So it is likely that the agglomerates start to be formed near the burning char where the formation of molten ash on the char surface is enhanced by high surface temperature of char particle; about 50-200 °C significantly higher than bed temperature, based on calculation. This molten ash on char surfaces causes char particle becoming sticky. As sand grains collide with the burning char particles, they may adhere to the char surface. Collision from bed mixing, however, can break this coherence and the remnant melt is left on sand surface. This is an important way of inorganic migration, namely the collision mechanism. If no breaking due to a local poor bed mixing, the formed hollow structure as the remaining ash skeleton from burnt out char would appear.

The melts migrating from the high temperature of char surface to the lower temperature of sand surface may be partly solidified; hence the partially molten coating layer occurs. Bed particles having the liquid phase presents on their surfaces has more inertia and tend to get close to the larger fuel char particles, and resultantly the continuous deposition of the additional melt on the limited sand surface extend the porous coating and finally the agglomerates are developed by the porous bonding necks with certain thickness. The agglomerate supported by thin necks may be formed by the rapid formation of the melt and the sudden adhesion. Other possible migration ways of inorganic elements to bed grain are condensation/deposition of inorganic gases/aerosol [69, 81], of which the evidences were given in Figure 5.16d. The diffusion of K in existing cracks or from surface of sand particle results in the formation of K-silicates toward the core of sand grains, as the compounds with higher thermochemical stability [69]. This material may partially be solidified at typical bed temperature and thus allows the additional K to diffuse through the early formed high porous silicate layer, accelerating a continuous widening of the attacking silicates formation. It should be noted that the diffusion of potassium is the rate determining step in the K-Silicates formation rate. This mechanism enhances the formation of the silicate melt and may be further responsible for the relatively high agglomeration tendency of palm bunch.

Two kinds of agglomerates could be observed in the same spent bed samples (Figs. 5.14b and 5.14c). Agglomerate with thin neck was composed to a great extent of two to four particles while agglomerate of a larger number of sand grains was supported by the larger amount of the melt, by the thicker layer or larger number of neck. Previous studies suggested that the adhesive force by the melt ash is strongly dependent on the amount and stickiness [109,160]. Agglomerate formed by large amount of the melt may require some certain resident time to develop the coating layer and neck while agglomerate supported by thin necks is suddenly formed by rapid formation of the melt [72]. The former agglomerate may thus appear in the bed at the early combustion stage while the latter, having a weaker structure, may dominate in the bed upon defluidization or otherwise in a local poor bed circulation zone, such as the corner of furnace chamber.

5.3.2 Pilot scale agglomerates

Typical agglomerate samples obtained from pilot scale experiments, including EDS analyses, were shown in Figures 5.18-5.22 during palm shell, corncob, palm bunch and rice straw combustion, respectively, in a pilot scale fluidized bed.

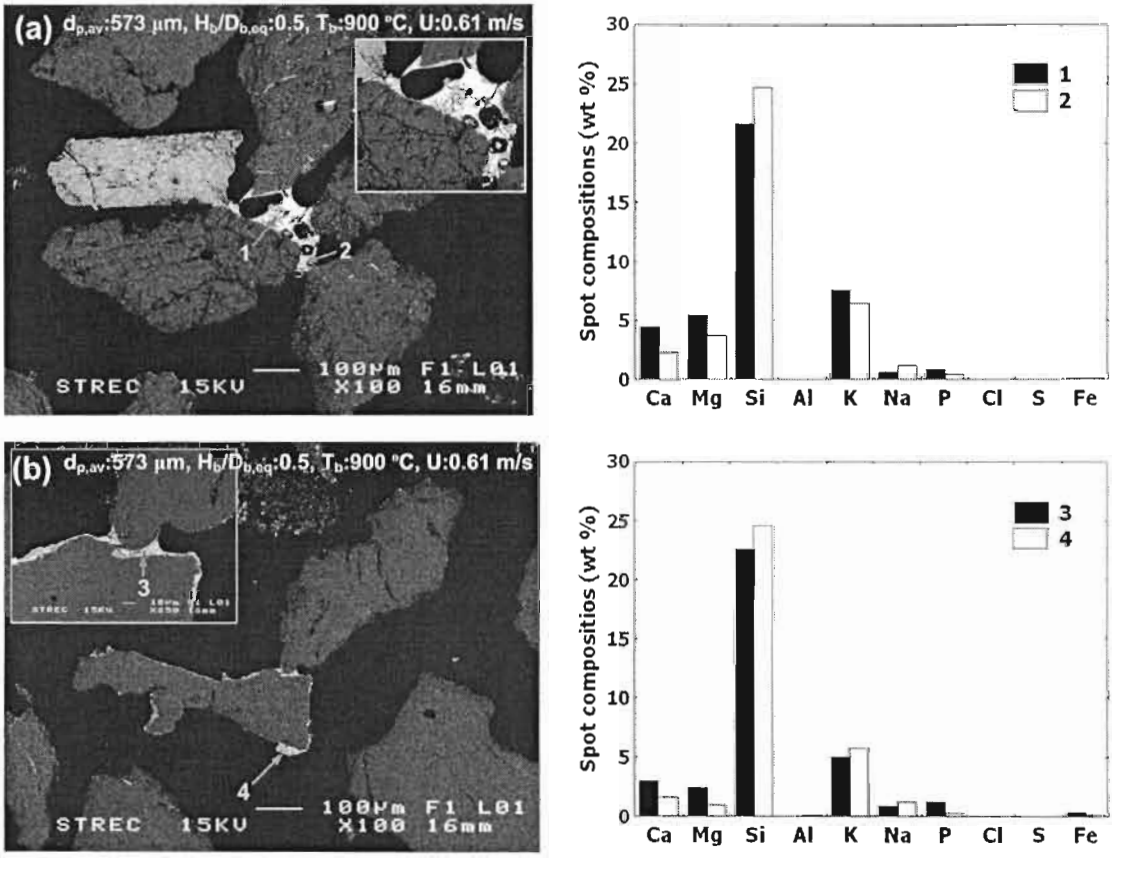

Figure 5.18 Typical SEM pictures and concomitant EDS elemental distributions of palm shell agglomerates from pilot scale FBC tests.

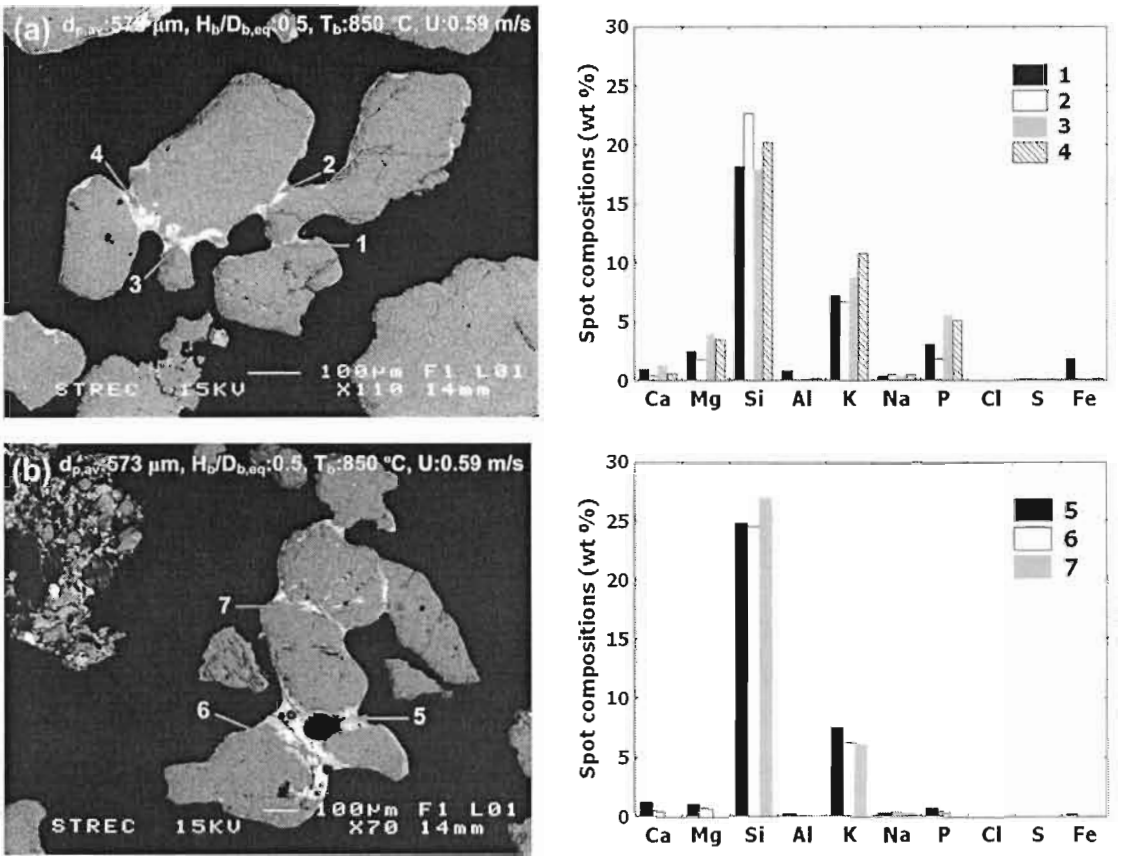

Figure 5.19 Typical SEM pictures and concomitant EDS elemental distributions of corncob agglomerates from pilot scale FBC tests.

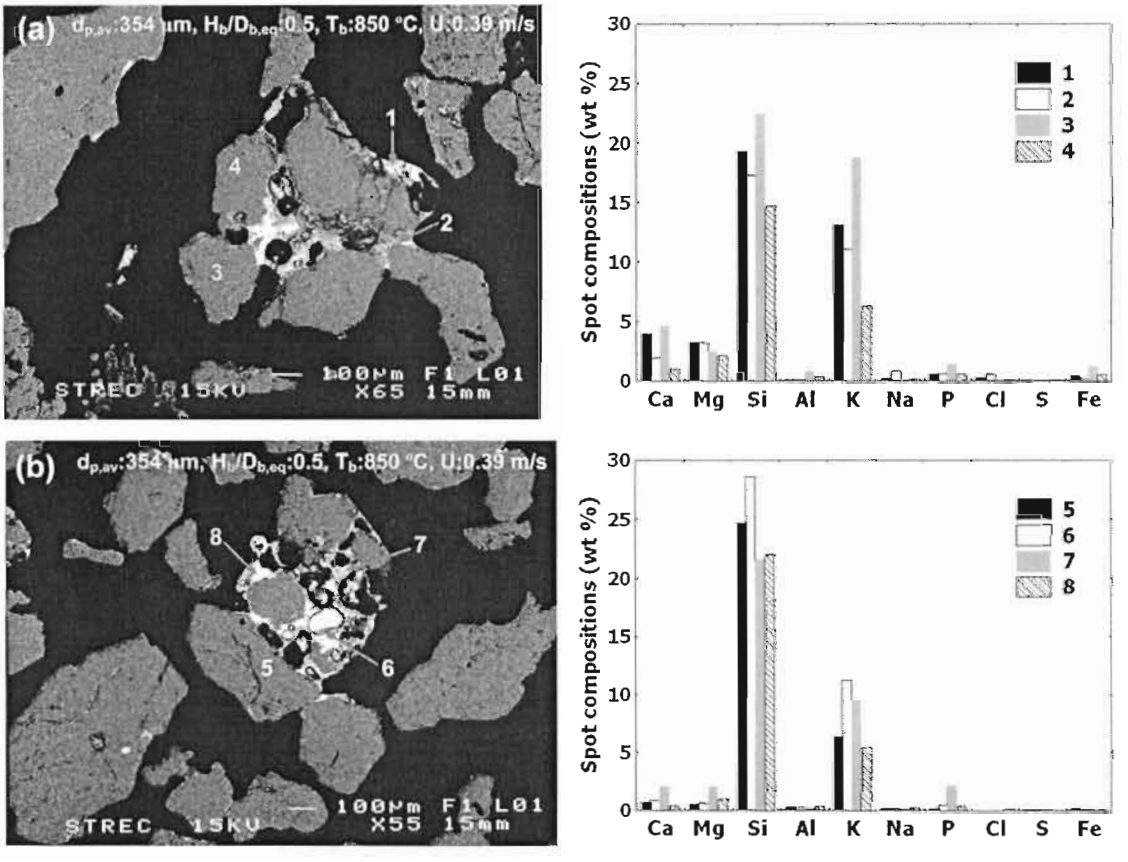

Figure 5.20 Typical SEM pictures and concomitant EDS elemental distributions of palm bunch agglomerates from pilot scale FBC tests.

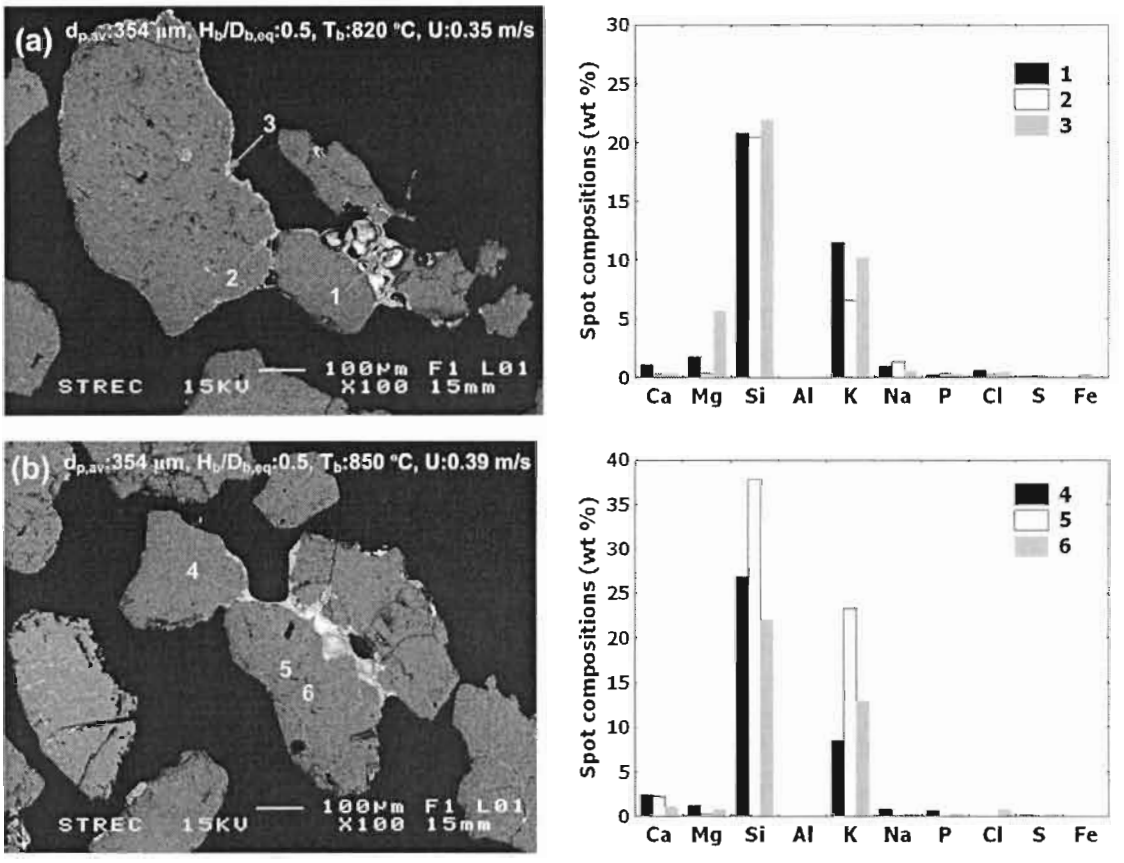

Figure 5.21 Typical SEM pictures and concomitant EDS elemental distributions of rice straw agglomerates from pilot scale FBC tests.

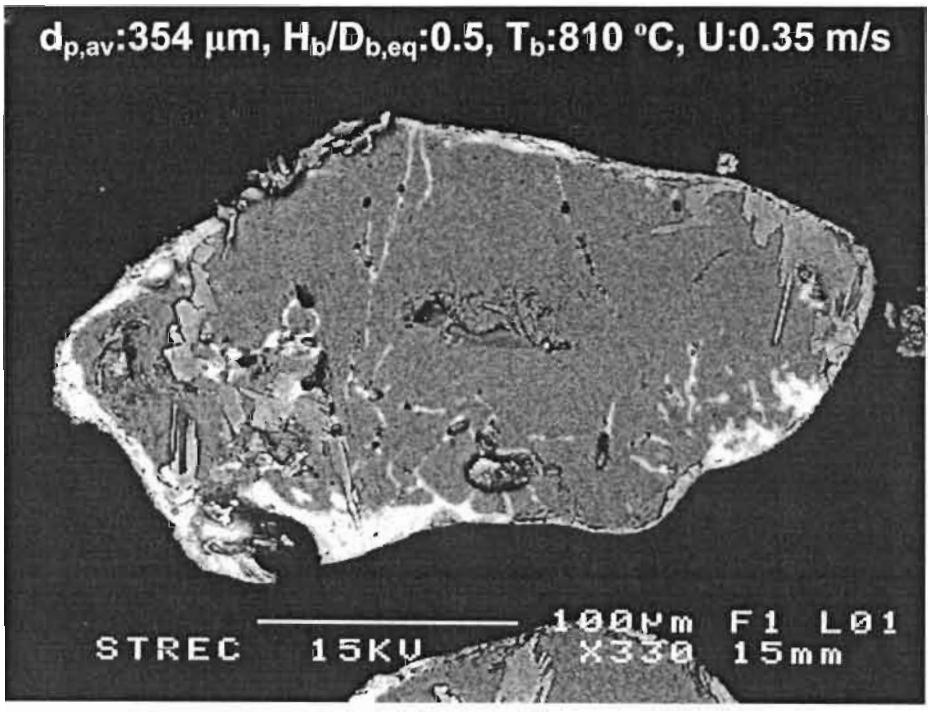

Figure 5.22 Illustration of the chemical attack inward quartz sand (Run No.4 of Table 5.7).

The features of agglomerate samples from pilot scale test were relatively similar to those from lab scale test. Agglomerates were formed likely by molten compounds as the neck and coating materials comprised of relatively rich Si and K; and Mg and Ca to a minor extent. They were likely the K-silicates. The relatively high P in corncob agglomerates was observed. S and Cl in very small fraction were also detected. Sand particles were adhered together by either bonding porous layer (Fig. 5.21b) or thin neck (Fig. 5.19a). The hollow structures located between bed particles (Fig. 5.20) or on the bed surface (Fig. 5.20a) were also observed. Non-homogenous coating and neck were common while relatively homogenous material was located between bed particles as thin layer neck. The diffusion and reaction propagating inward the quartz particle by gaseous potassium compounds or potassium containing aerosols, in existing cracks or from sand surface, was noticed typically as showed in Figure 5.22. This resulted in the presence of K silicates inside bed grains.

In the present work, the migration of ash forming constituents from fuel particle to bed particle was likely dominated by the collision. Condensation / aerosols deposition as parallel migration mechanisms showed an increasing degree, if K-gaseous and aerosol facilitators, namely Cl and S respectively, presented at relatively high content in biomass. It could be further concluded from the mentioned results that the bed agglomeration process was the reactor scale independent.

By the above SEM investigation, the mechanism which supposedly functions at relatively low temperature could be discerned in Figure 5.23.

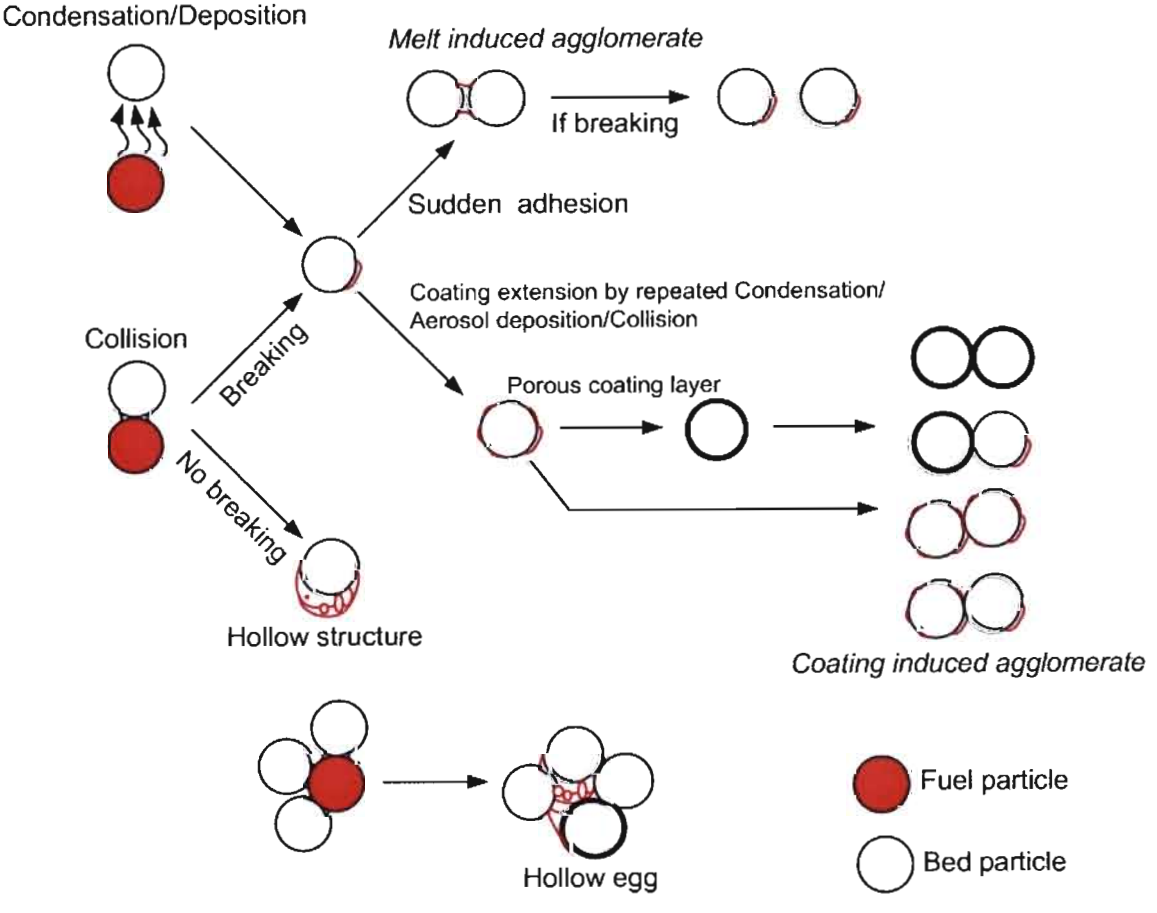

Figure 5.23 Suggested mechanism of the agglomerate formation

5.4 Thermodynamic behaviors of biomass ash under FBC conditions

In order to describe the presence of an individual ash forming element to the formation of fused material as coatings and necks, all EDS data including initial biomass ash for comparison were summarized to a set of plots showed in Figure 5.24.

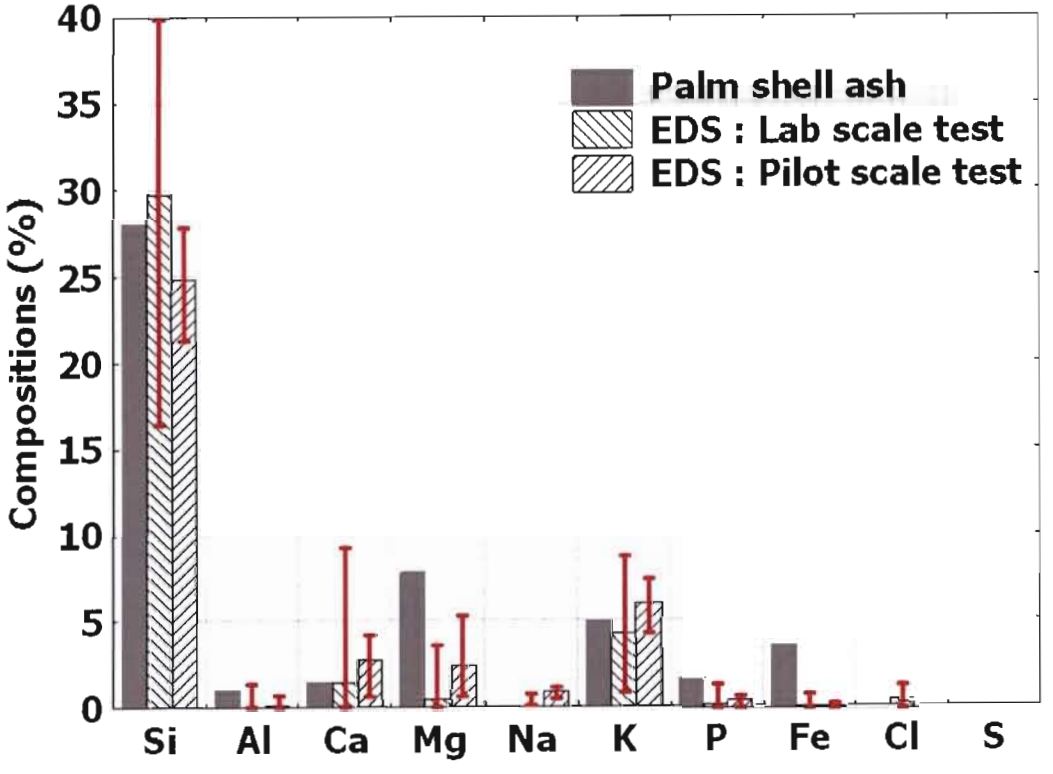

(a)

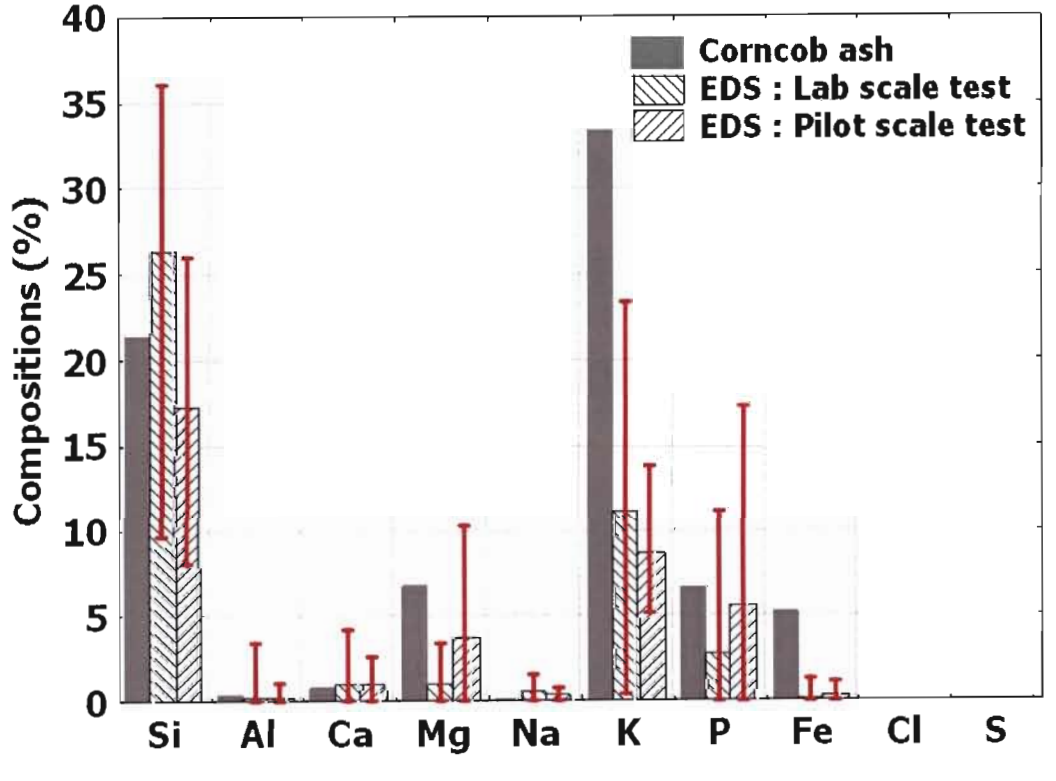

(b)

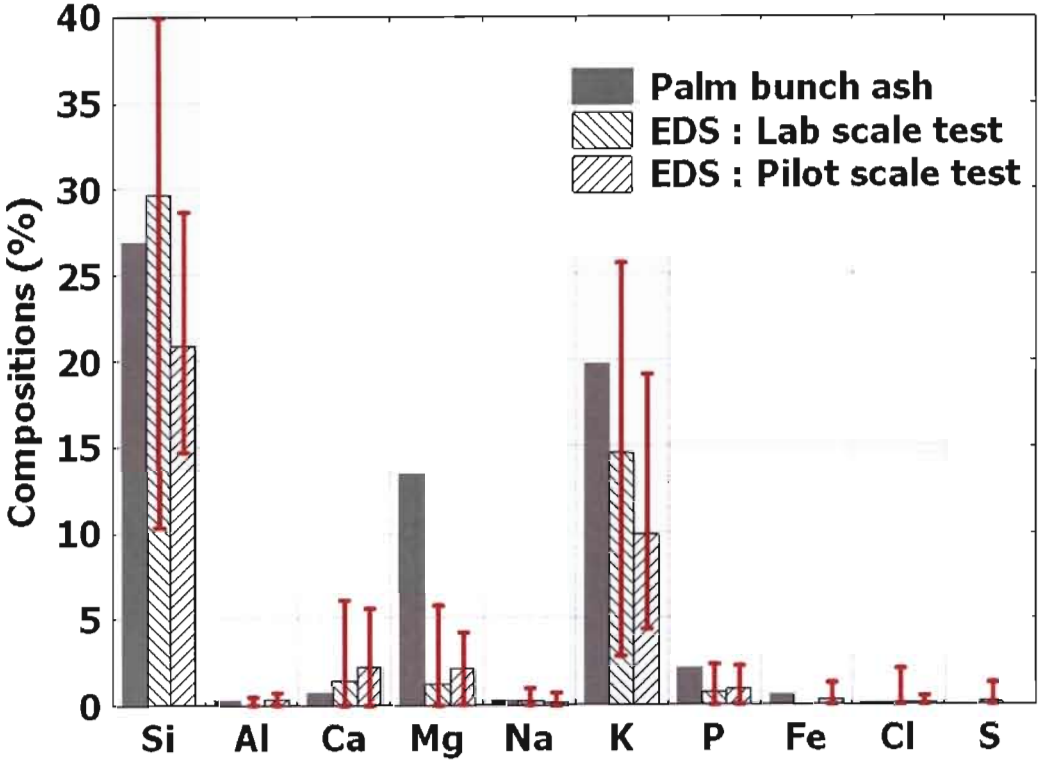

(c)

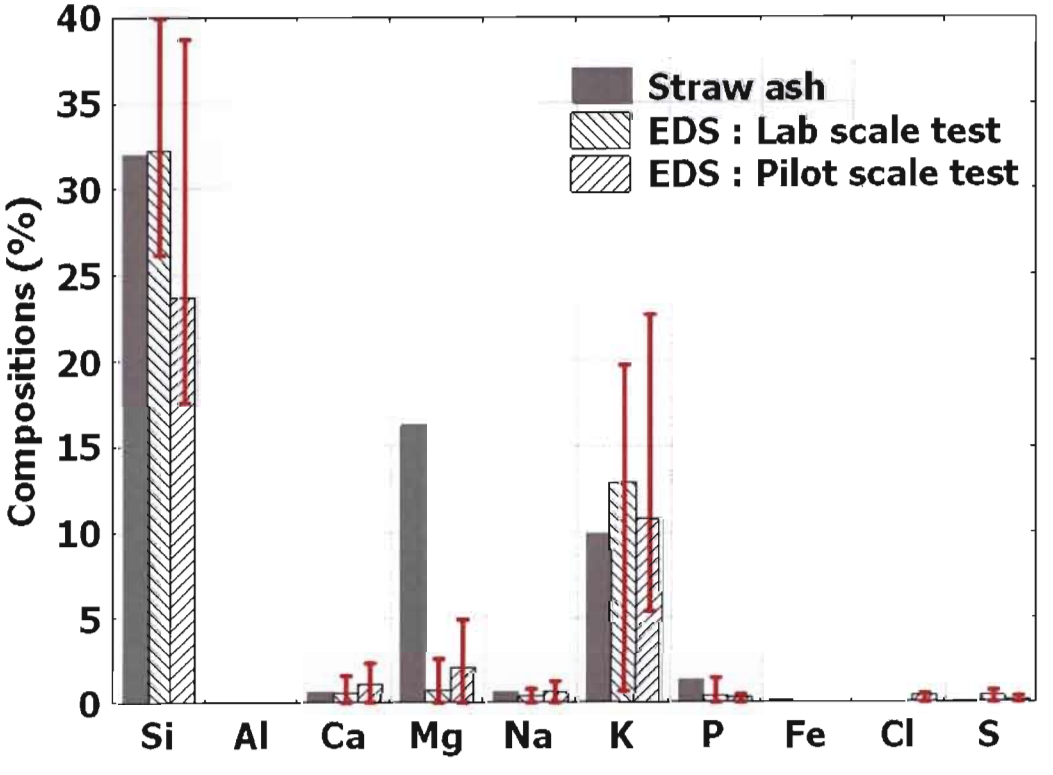

(d)

Figure 5.24 Distribution of elements in the initial biomass ash and EDS analysis of fused materials of agglomerates formed from burning (a) palm shell, (b) corncob, (c) palm bunch, and (d) rice straw in lab and pilot scale FBC.

In Figure 5.24, the distribution of elements in fused materials was widely, indicated by the vast ranges of error bars. The average compositions of fused materials were close to that of the biomass ash, confirming that the coating and neck were originated from fuel. Si and K were the two major elements; Si was proved to be the dominant element in fuel ashes and fused materials. The average P contents in agglomerates were relatively lower than those of fuel ashes. Na, Al, Fe, Cl and S content in fused materials were insignificant. It was further noticed in Figure 5.24 that despite its relatively large in fuel ash, Mg content in agglomerates was quite small; this indicates that Mg may not be included in the melt formation. On the other hand, Ca may be included in the fused material compositions due to its higher content in coating and necks of agglomerates against with the fuel ash.

In K and Si rich and Ca poor system like the chemistry of corncob, P species as $K_4P_2O_7$ (M.P.: 1109 °C), K_3PO_4 (M.P.: 1340 °C) or P-Si compounds (M.P. > 1150 °C) may be the major fine particle products [76]. This presumption of P was also corroborated by a result of a previous SEM/EDX study [177] which revealed that the major P was arrested in the deposited fine ash, instead of the molten ash. Mg as a free fine particle of high melting point oxide salt (MgO: M.P. 2852 °C) [53,178] is the major form in an oxygen rich environment at high temperature combustion. This is verifiable that Mg species may include to a lesser extent in the molten phase dominated by the significantly lower melting point K-silicates.

In the silica rich system as found in FBC with quartz bed particles, the onset of the bed agglomeration can be attributed to the melt of K-salts or K-silicates whereas Si in molten materials may be derived from the fuel itself or bed material [24,69]. K species mainly released during char combustion are mostly retained in the bed where they are transformed to K-silicates while S and Cl do not participate in final agglomeration process [69]. The present EDS results showed an agreement to these explanations. However, the insignificant fraction of Cl and S detected in agglomerates may be derived from the chloride and sulphate salts of alkali earth group in alkali lean system [61].

From the above chemical analyses, Si and K were the two major abundant elements. Possibly Ca was in part of the melt formation. To examine the thermodynamic behaviors of fused materials, all EDS data including fuel ash compositions were normalized and then plotted on the K_2O-CaO-SiO_2 ternary phase diagram [179] as illustrated in Figures 5.25 and 5.26, for lab scale and pilot scale samples, respectively.

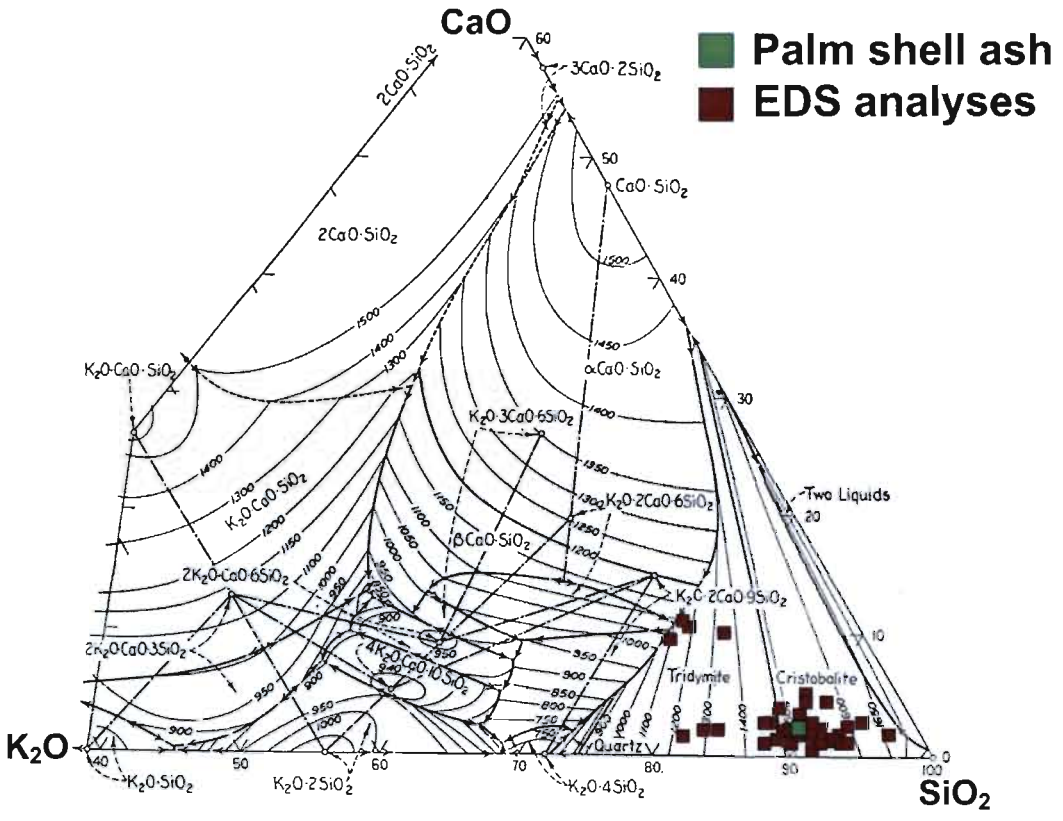
CaO
Palm shell ash
EDS analyses
3CaO·2SiO2
2CaO·SiO2
CaO·SiO2
αCaO·SiO2
βCaO·SiO2
K2O·CaO·SiO2
K2O·3CaO·6SiO2
K2O·2CaO·6SiO2
2K2O·CaO·6SiO2
2K2O·2CaO·9SiO2
2K2O·CaO·3SiO2
4K2O·CaO·10SiO2
Two Liquids
Tridymite
Cristobalite
Quartz
K2O·SiO2
K2O·2SiO2
K2O·4SiO2
K2O
SiO2

(a)

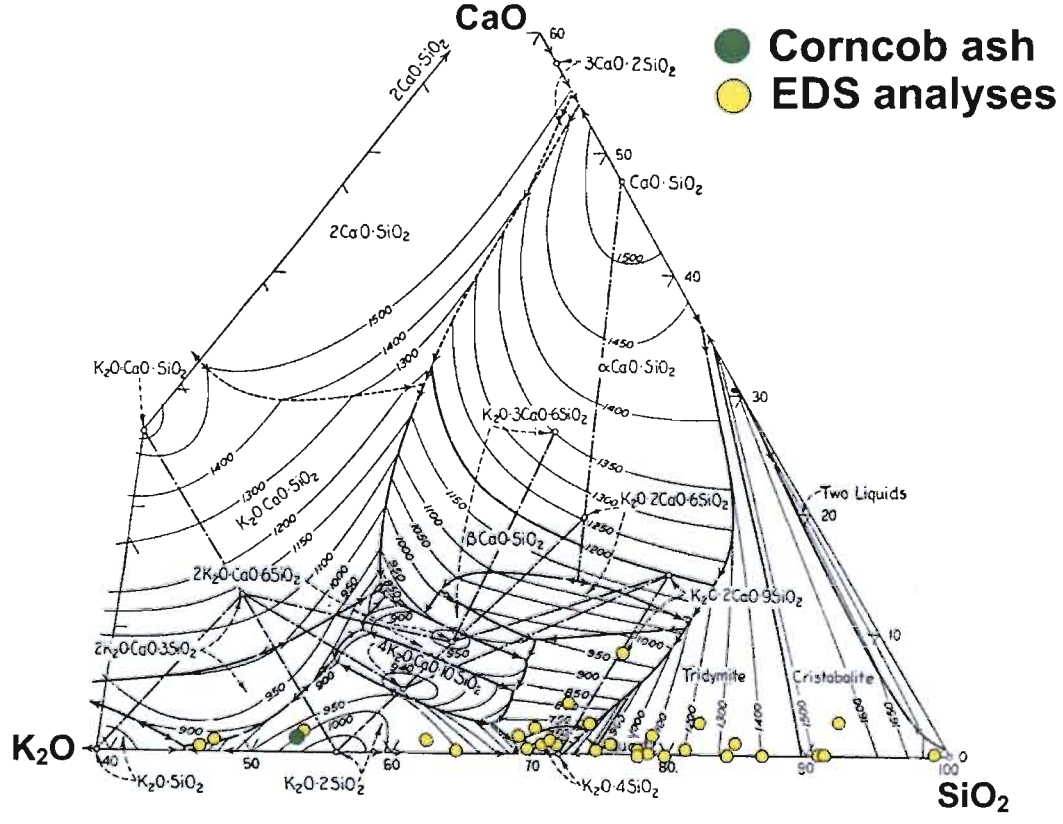
CaO
Corncob ash
EDS analyses
3CaO·2SiO2
2CaO·SiO2
CaO·SiO2
αCaO·SiO2
βCaO·SiO2
K2O·CaO·SiO2
K2O·3CaO·6SiO2
K2O·2CaO·6SiO2
2K2O·CaO·6SiO2
2K2O·2CaO·9SiO2
2K2O·CaO·3SiO2
4K2O·CaO·10SiO2
Two Liquids
Tridymite
Cristobalite
K2O·SiO2
K2O·2SiO2
K2O·4SiO2
K2O
SiO2

(b)

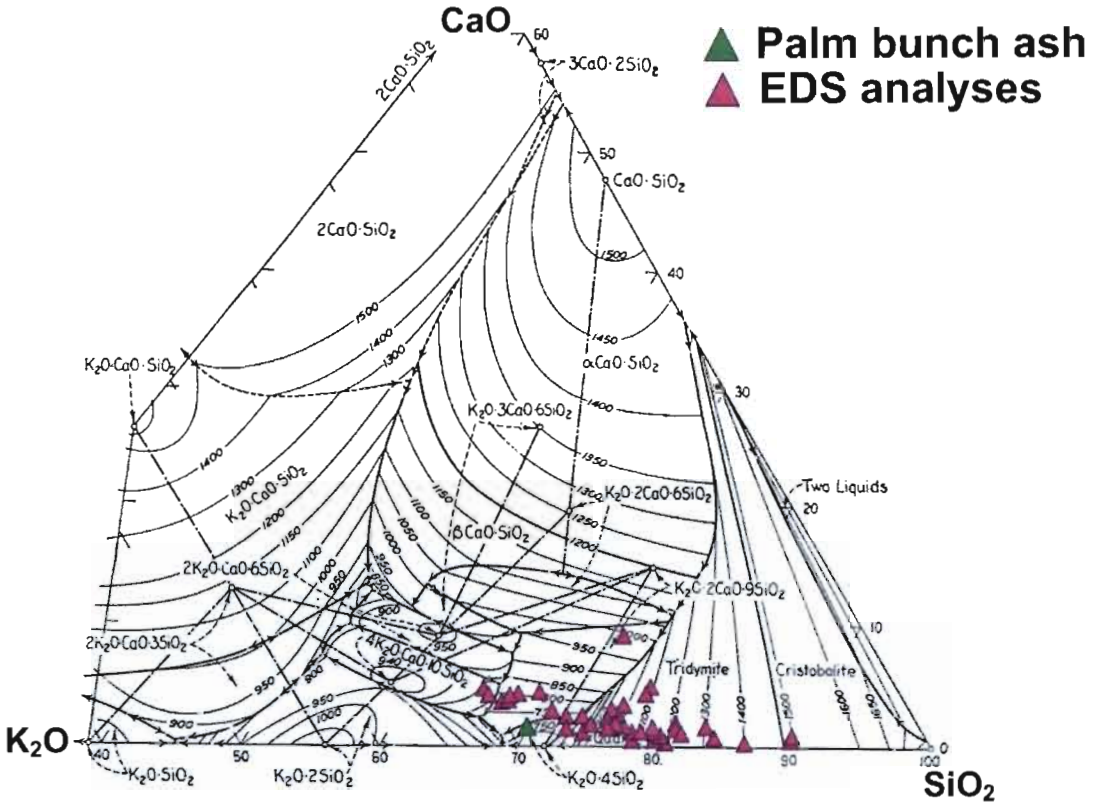

(c)

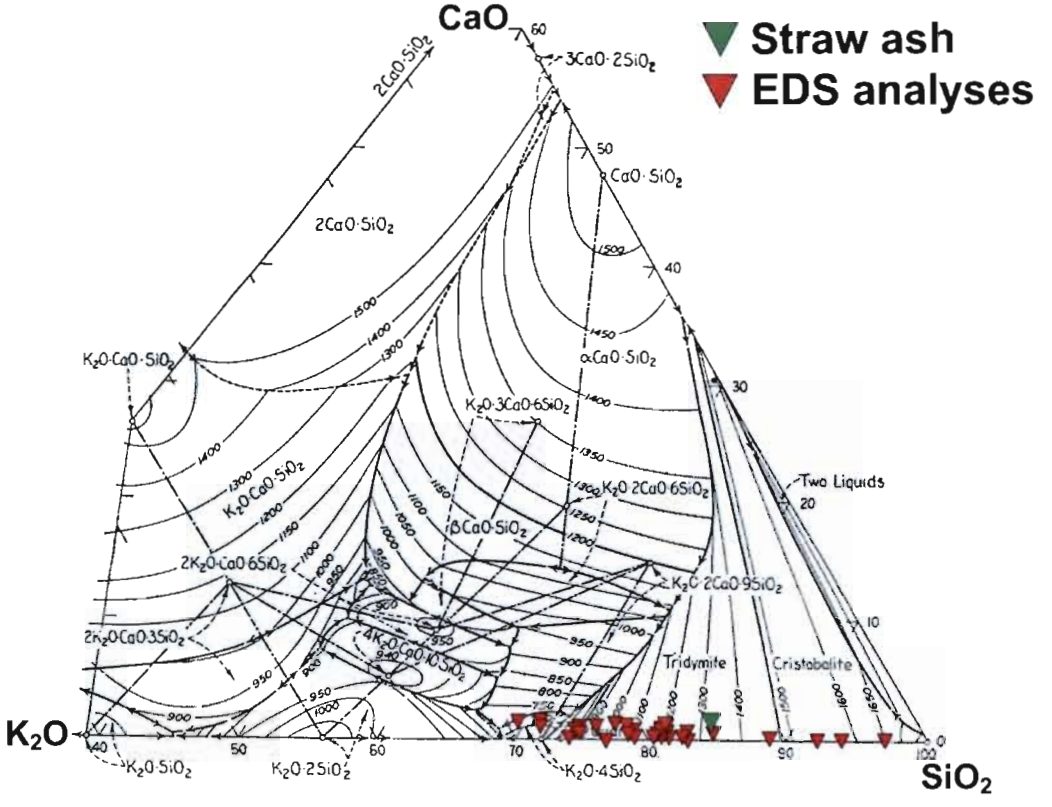

(d)

Figure 5.25 The simplified compositions of fused material from four biomass lab scale test and fuel ashes plotted in the K_2O-CaO-SiO_2 ternary phase diagram.

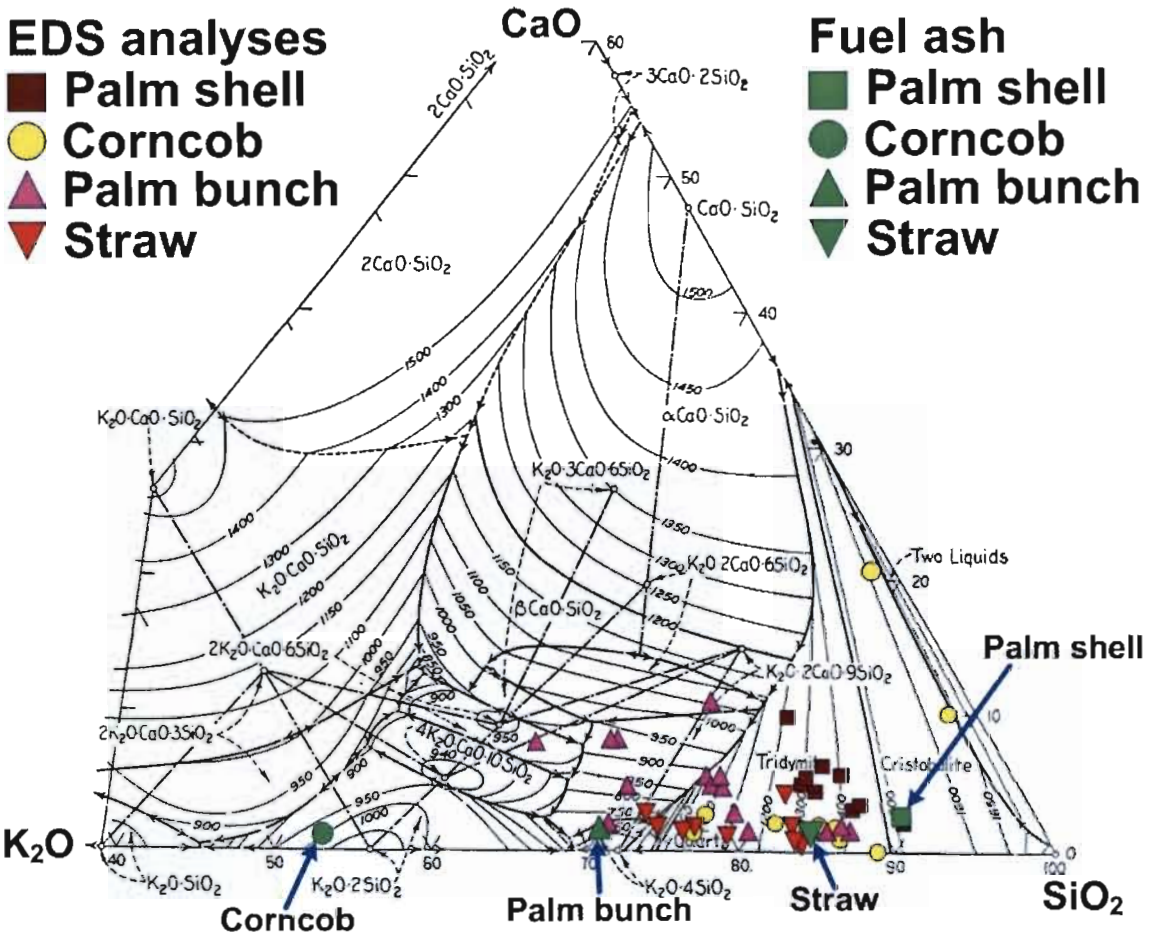

Figure 5.26 The simplified compositions of fused matters from pilot scale test and fuel ashes plotted in the K_2O-CaO-SiO_2 ternary phase diagram.

In Figure 5.25, they revealed that the compositions obtained from the lab scale agglomerate samples were mainly located to the SiO_2 rich and CaO poor region; especially those of palm shell agglomerates were mostly restricted to the SiO_2 rich corner and relatively close to the fuel ash composition (Fig. 5.25a). K_2O contents in agglomerates were widely distributed (palm shell: 5-15 %, corncob: 6-36 %, PEFB: 10-38% and rice straw: 15-29%). The compositions of fused materials in corncob, palm bunch and rice straw agglomerates were mainly located in the area where the eutectic with an initial melting temperature about 740 °C was nearby, while those of palm shell agglomerate were mainly in the zone of relatively higher liquidus temperature about 1200-1400 °C (*liquidus temperature is the minimum temperature at which all components of a mixture can be in a liquid state. Below the liquidus, the mixture will be partly or entirely solid*) [179]. The high K content can form the wide composition ranges of amorphous material and the wide distribution of EDS composition indicates to the poor elemental distribution of forming ash in fluidized bed.

The similar trends were also observed (Fig. 5.26) from the examination of pilot scale agglomerates. The simplified EDS compositions were so widely distributed but mainly located in the area, where the eutectic compositions with 740°C of an initial melting point were nearby. It is due to the fact that the fuel ash is the mixture of multi inorganic compositions giving the wide range of melting temperature. Previous works [106,128] had indicated that the chemical characteristics and thereby the melting of material at

coatings are significant for bed agglomeration process. If the coating has a high enough fraction of molten phase, it will cause bed agglomeration. The fraction of the melt needed for stickiness has been determined for silicate melts [92]. Therefore it was of interest in this study to determine the melting behavior of different fused material compositions. The fractions of the melt as a function of temperature at typical EDS compositions (in Figs. 5.14 to 5.21) were extracted from phase diagram by the well defined "Lever rule" and shown in Figures 5.27 and 5.28 for lab scale and pilot scale examination, respectively.

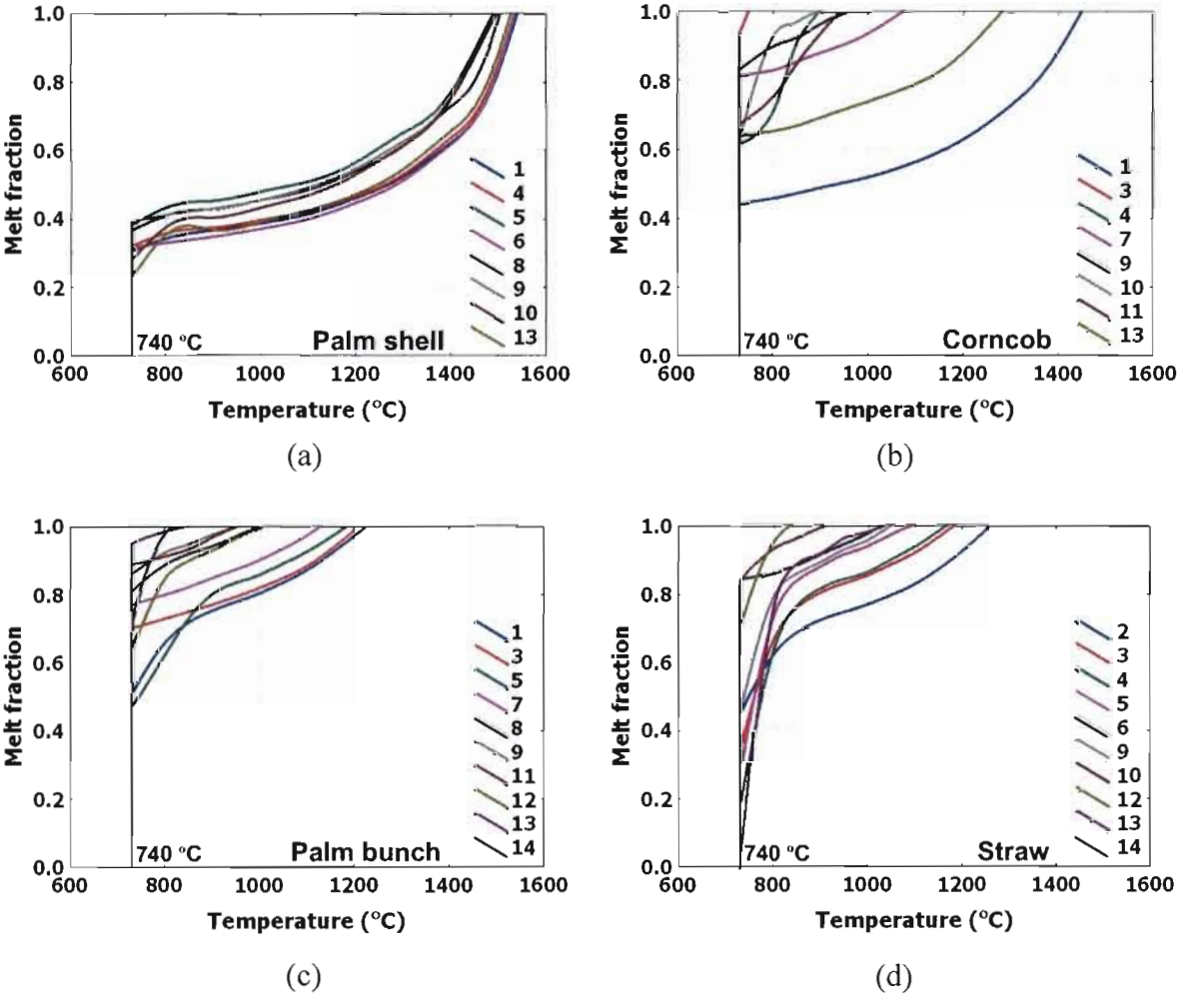

Figure 5.27 Typical melting behaviors at specific spot characteristics of fused material of agglomerates created from burning (a) palm shell, (b) corncob, (c) palm bunch, and (d) rice straw in a lab scale FBC (No. of lines correspond to EDS spots in Figure 5.14 to 5.17, respectively).

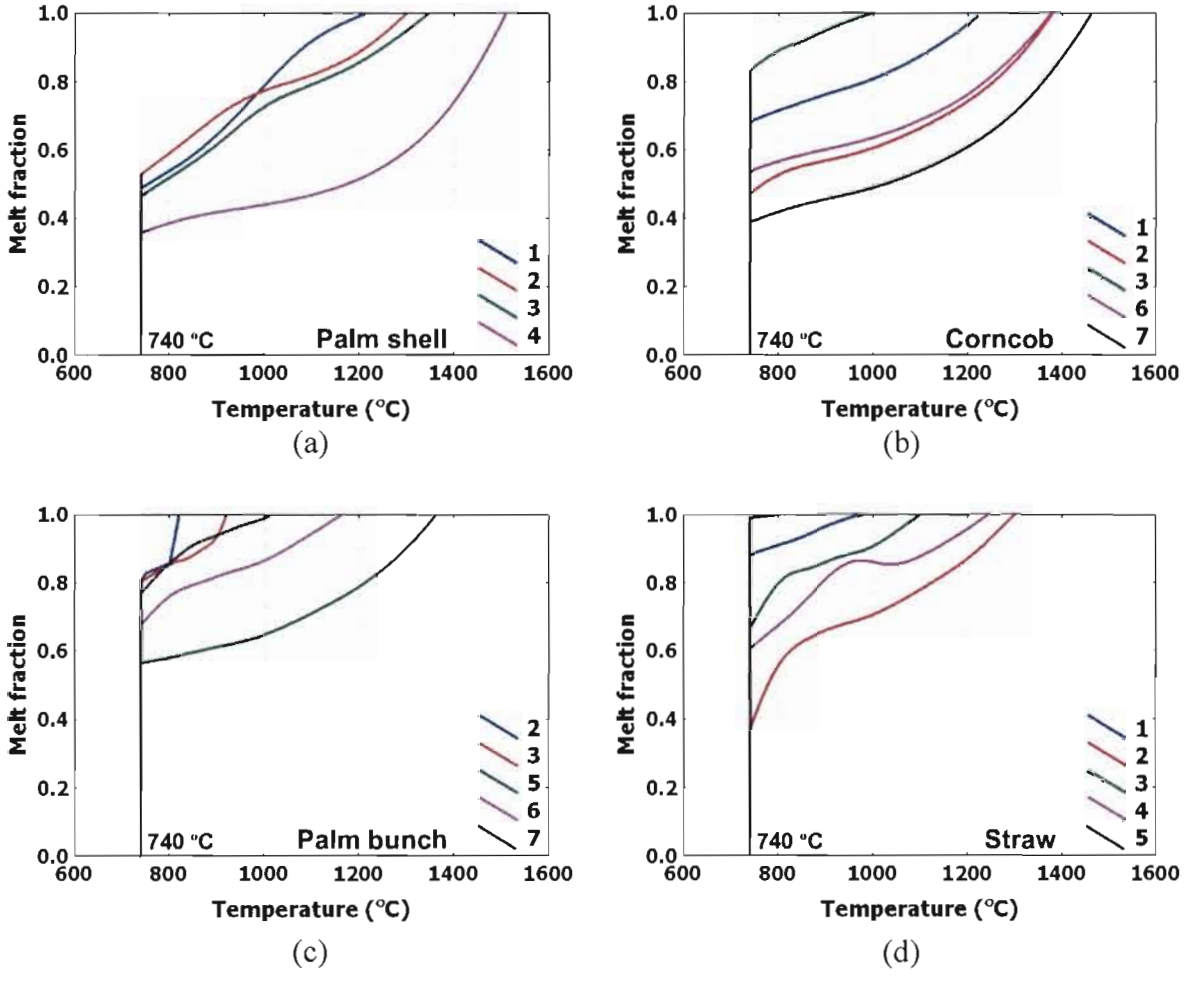

Figure 5.28 Typical melting behaviors at specific spot characteristics of fused material of agglomerates created from burning (a) palm shell, (b) corncob, (c) palm bunch, and (d) rice straw in a pilot scale FBC (No. of lines correspond to EDS spots in Figure 5.18 to 5.21, respectively).

It revealed from the results of lab scale test (Fig. 5.27) that the melting behaviors of the Ca lean system in this study were very sensitive to the amounts of K in the samples. All fused materials had an initial melting point about 740 °C. The melt profiles were relatively similar for corncob, palm bunch and rice straw agglomerates, even though that of rice straw agglomerates slightly differed at temperature of 740-840°C at which the relatively lower melt fraction had been estimated (Fig. 5.27d). Estimated fraction about 50-94 wt% of fused materials with relatively large potassium content, of corncob and palm bunch agglomerates, could melt at temperature as low as the initial melting temperature, while more than 50 wt% of fused materials in palm shell agglomerates would melt at temperature well above 1200 °C (Fig. 5.27a). Fused materials in corncob, palm bunch and rice straw agglomerates contained 60-95 wt% of melt fraction at low temperature as 800 °C, approximately.

The relatively similar trends were noticed in the estimation of melt fraction of pilot scale agglomerates illustrated in Figure 5.28. The higher fraction (40-90 wt%) of corncob, palm bunch and rice straw fused materials became to molten phase at an initial melting point, while palm shell fused materials were transformed to a liquid phase at relatively lower fraction (35-50 wt%). The aforementioned behaviors also confirmed the reactor scale independence in the bed agglomeration process.

The above results seemed to confirm that the partial molten phase formation in the released ash was responsible for the agglomeration, and it could be enhanced by the high surface temperature of burning char. The compositions of potassium silicate fused materials close to the eutectic mixture, caused by the high alkali content in fuel, yielded the greater melt fractions, at the same temperature range, giving the high bed agglomeration tendency. It should be noted that the fused materials in agglomerates analyzed above are the result of two competitive mechanisms as shown in Figure 5.23, and their influences are taken into inseparable consideration by the phase diagram analysis.

5.5 Mathematical model prediction and verification

The two mathematical models developed in Chapter 4 were verified by the present experimental results and the previous published experimental data.

5.5.1 A newly developed model

In this section, the prediction and verification of a newly proposed model was reported and discussed.

1. Model analysis

A present mathematical model mentioned in Chapter 4 was

$$\left(\frac{m'_{fuel}.t_{def}}{m_{bed}}\right) = B0*\left(\frac{\mu_l}{\mu_g}\right)^{B1}\left(\frac{U}{U_{mf}}\right)^{B2}\left(\frac{d_p}{D_b}\right)^{B3}\left(\frac{H_b}{D_b}\right)^{B4}\left(X_{melt}\%ash\right)^{B5} \tag{4.14}$$

The analytical results from MLR analysis, using the lab scale data in Table 5.5, described by the expression of Equation 4.14 were summarized in Table 5.8.

Table 5.8 Constants and contribution of independent dimensionless groups

Dimensionless term	Constant	β
	0.032 (B0)	-
Viscosity	0.360 (B1)	0.489
Fluidizing velocity	1.071 (B2)	0.188
Particle size	0.916 (B3)	0.121
Static bed height	-0.028 (B4)	-0.006
Ash melt fraction	-1.035 (B5)	-0.650

where beta coefficient (β) is the magnitude, the value between 0 to 1, indicates directly the intercomparable contribution; the higher Beta value, the higher influence. The negative implies the inverse form of the defined dimensionless term. The comparative results in Table 5.8 showed clearly that the characteristic of inorganic constituent in fuel and temperature which contributed to the development of the viscous ash melts were the major contribution to the bed agglomeration behaviors, while the bed conditions such as air velocity, bed particle size and static bed height showed minor. The velocity affected at relatively higher on the segregation in fluidized bed than the particle size, while the bed height showed a less significant effect. The velocity, particle size and melt fraction was quite in the linear relationship to t_{def}. The order of inverse melt quantity group (B5) was proved to 1, which corresponded to a model assumption, in Chapter 4.

This model analysis provided the firmly consistent description to the results of this present work and previously reviewed studies which clearly indicated the highly significant influences of the fuel ash chemistry and temperature and that the melt formation controlled the bed agglomeration.

The degree of mixing in fluidized bed relative to the breaking and collision is contributed mainly by the gas velocity [34,147,148]. The early mathematical models [109,166] proposed the half order of excess velocity ($U-U_{mf}$) to t_{def} by the regression analysis, while the above analysis indicated differently as the linear function (B2). Furthermore, approximately first order of bed particle size effect (B3) was presently revealed while the early works proposed variously (Lin et al [109] = -0.5 and Lin et al [166] = -0.25). The order of inverse melt quantity group (B5) was proved to 1, due to the direct mass calculation of ash feed. This was corresponding to the order of the inverse alkali feed rate group, relative to t_{def}, in the model formulated by Lin et al [166], while an early model [109] set this order to 0.5.

2. Model verification

The t_{def} prediction by a model of Equation 4.14 on the lab scale combustion data was showed in Figure 5.29. The predictive result followed the experimental data with a fairly good agreement, since they were the source of regression analysis. The error calculation ranged ±21%, showing satisfactory.

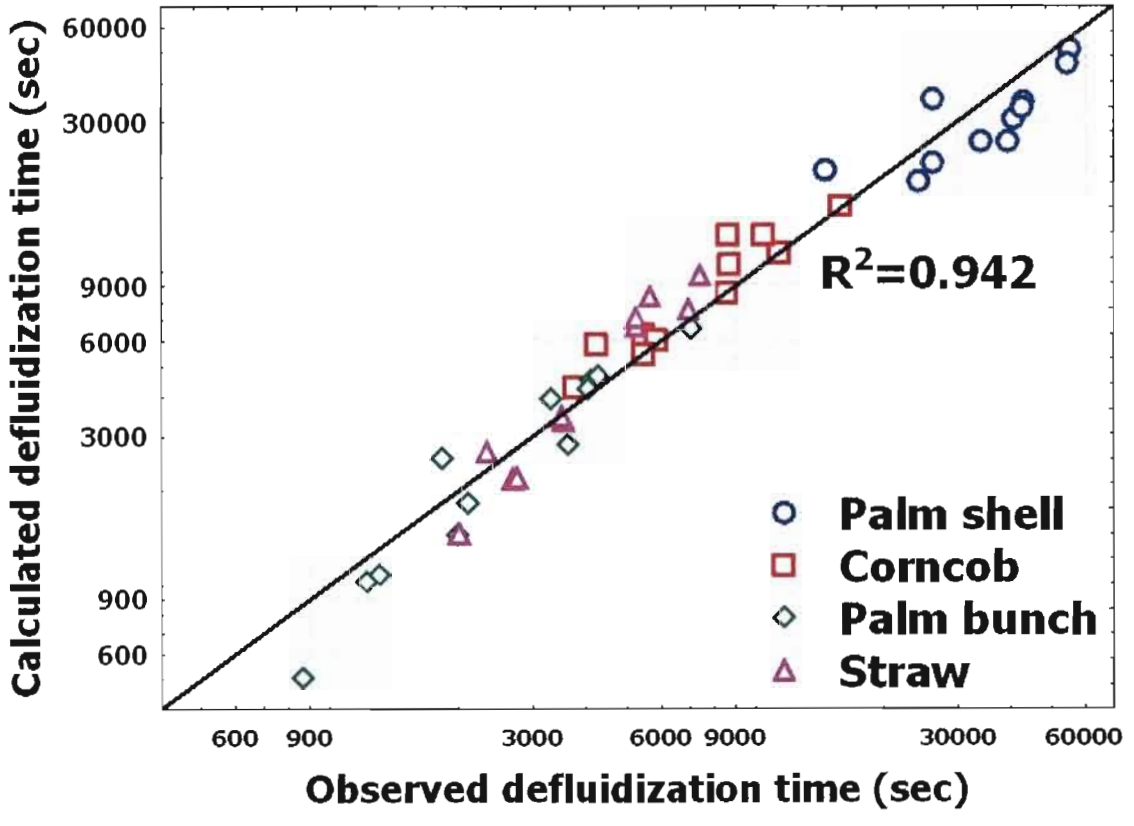

Figure 5.29 Comparison of calculated defluidization time with lab scale results.

To further verify the ensured accuracy of this model, the predictions of t_{def} from the conditions of pilot scale experiments of this study and previous bed agglomeration works performed experimentally with several kinds of biomass residues were carried out. Their predicted results with pilot scale and previously published data were illustrated in Figure 5.30a and 5.30b, respectively, and showed fairly well in consistence. In Figure 5.30b, the predictive results in the form of the dots with bands indicated the calculated average and reported range of straw feed rate in some conditions of wheat straw combustion [109,149]. The straw blends were the biomass mixture of rice straw and the defined commercial fuel (80% wood + 20% almond shell) [146].

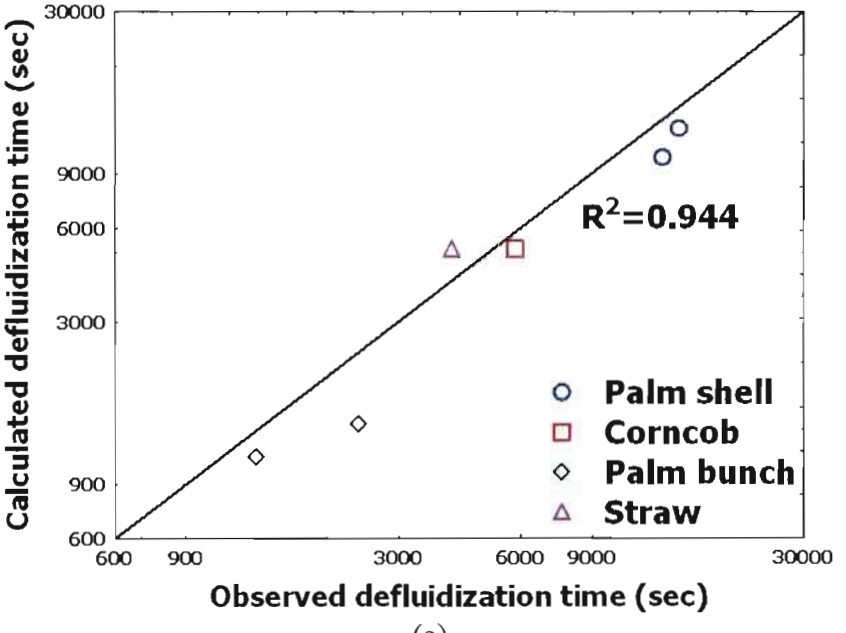

(a)

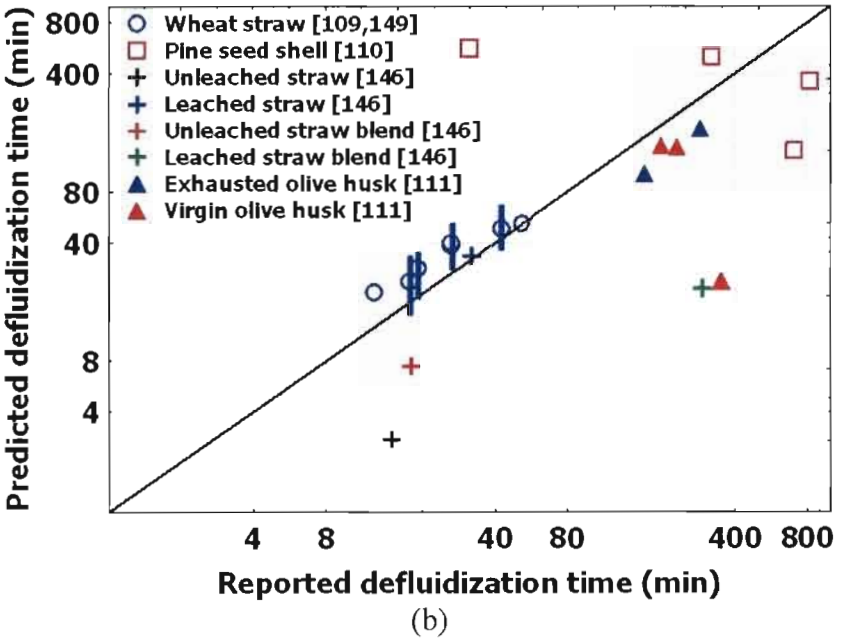

(b)

Figure 5.30 Verification of model with (a) the pilot scale results and (b) the previous published data.

5.5.2 A modified model

1. Model analysis

A model which was modified from the original model of Lin et al [109] to predict t_{def} was proposed as an optional model in Equation 4.25 viz;

$$t_{def} = C_{new}\left(\frac{m_{bed}}{m'_{fuel}\,X_{ash}X_{K.in.Ash}}\right)^{A}\left(\frac{U-U_{mf}}{d_p}\right)^{1/2}\exp\left(\frac{E_\mu}{2RT_b}\right) \quad (4.25)$$

A set of lab scale data were analyzed by using the linear regression technique to calculate C_{new}, A and E_μ of an individual biomass as following,

- A slope of the line plotted between t_{def} and inverse bed temperature in logarithm scales indicated the viscosity activation energy (E_μ).
- For each biomass at constant bed temperature, the logarithmic plot between t_{def} and the mass ratio group provided A constant, as the slope of the line.
- Finally, C_{new} was a slope calculated by plotting t_{def} in linear scale against with the group parameters on the right side of Equation 4.25 with corresponding A and E_μ, as the linear equation.

The regression results were summarized in Table 5.9, including the previously published data and prediction of original model (Eq. (4.23)) with lab scale data.

Table 5.9 Model parameters

Biomass	**A**	**C [Eq. (4.23)]**	**C_{new} [Eq. (4.25) at A=1]**	**E_μ/R (K)**
Palm shell	0.90	3.77×10^{-4}	1.04×10^{-3}	33,670
Corncob	1.12	1.81×10^{-3}	2.61×10^{-11}	27,340
Palm bunch	0.82	3.92×10^{-3}	2.25×10^{-8}	21,741
Rice straw	0.92	1.35×10^{-1}	7.52×10^{-8}	16,492
Wheat straw [109]	***0.5***	$\mathbf{1.11 \times 10^{-4}}$	$\boldsymbol{2.67 \times 10^{-10}}$	**29,000**

It was noticed that A, an order of the mass ratio group, were around 0.82 to 1.12 and close to 1, which was similar to B5 of Equation 4.14 in Table 5.8, while 0.5 was early set in an original model. Therefore, all A were set newly to 1 to determine C_{new} by the subsequent regression. Among the observed biomass, E_μ/R and C_{new} of palm shell showed the highest value. E_μ/R of the present biomass showed relatively similar order of magnitude to that of the wheat straw from a previous work [109].

2. Model verification

The C_{new} and E_μ/R in Table 5.9 obtained in this way were then applied to calculate t_{def} for comparison, and the t_{def} comparative results were then illustrated in Figure 5.31, including the prediction by original model.

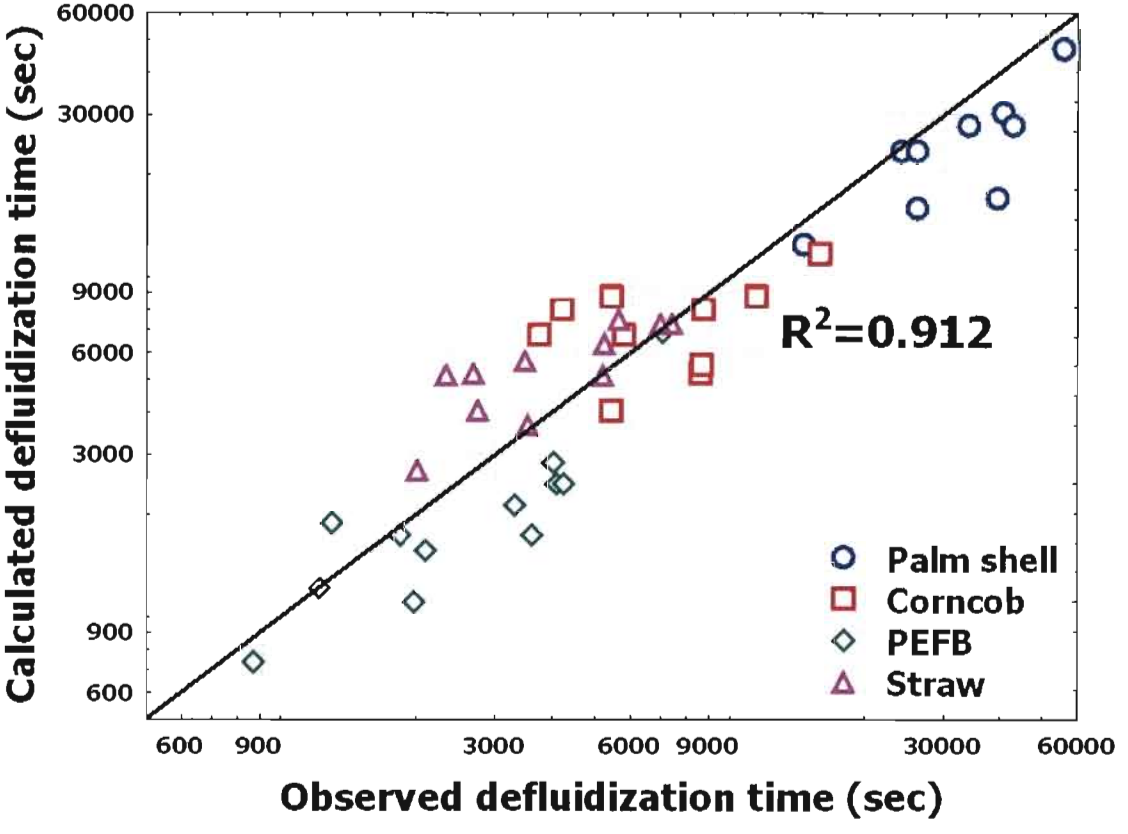
Calculated defluidization time (sec)
60000
30000
9000
6000
3000
900
600
600
900
3000
6000
9000
30000
60000
Observed defluidization time (sec)
R²=0.912
Palm shell
Corncob
PEFB
Straw

(a)

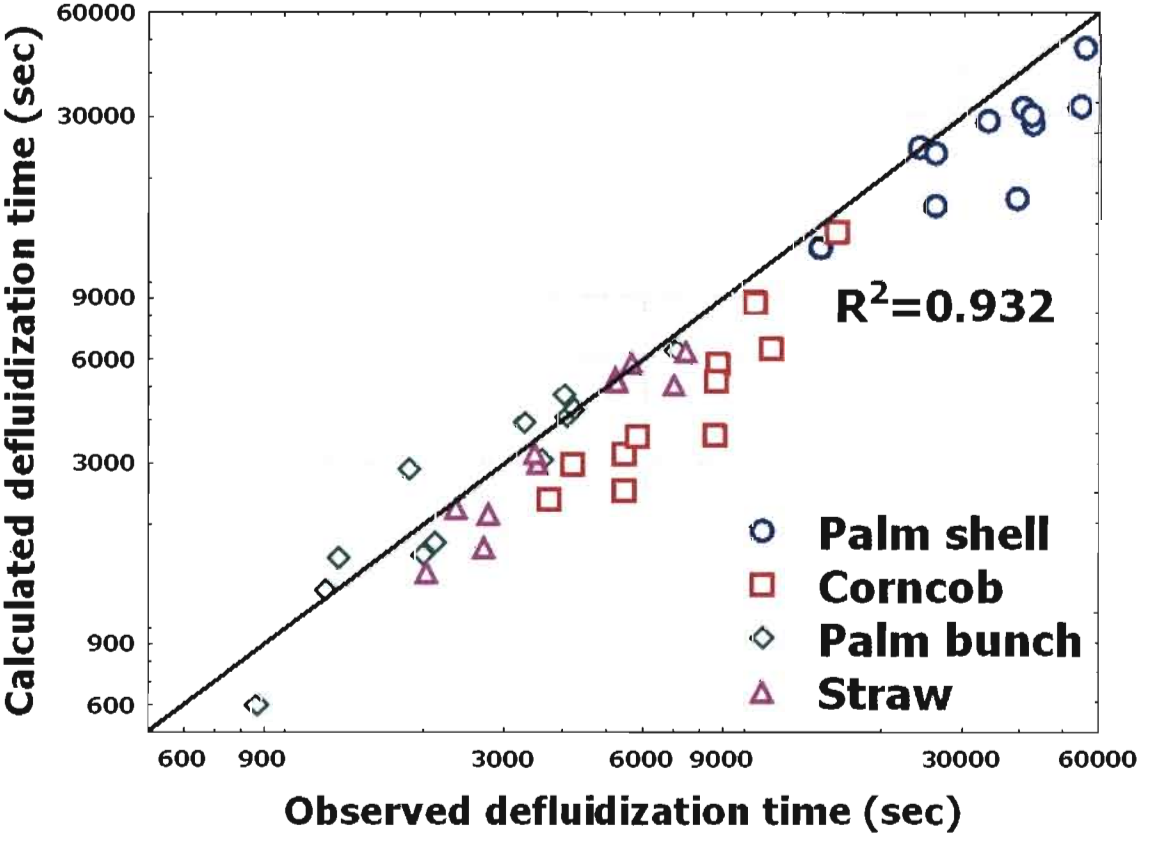
Calculated defluidization time (sec)
60000
30000
9000
6000
3000
900
600
600
900
3000
6000
9000
30000
60000
Observed defluidization time (sec)
R²=0.932
Palm shell
Corncob
Palm bunch
Straw

(b)

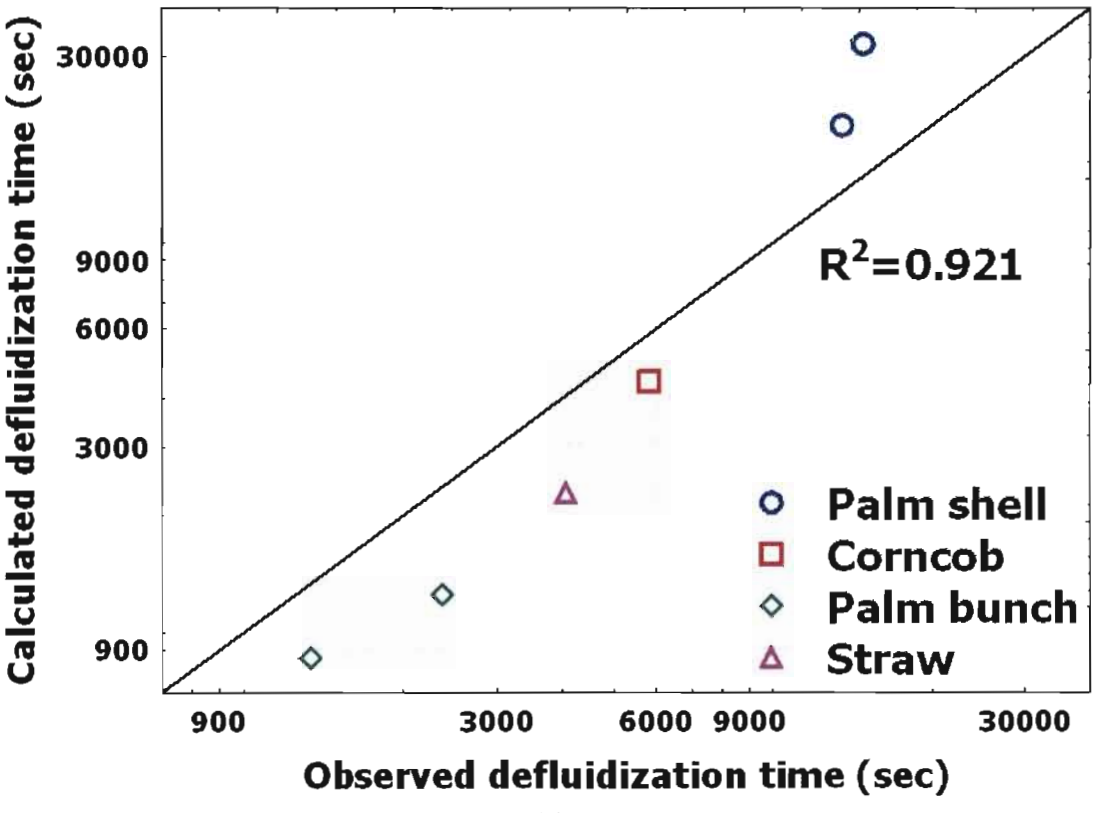

(c)

Figure 5.31 t_{def} comparisons with experimental data by; (a) Original model (Eq. (4.23)) with lab scale data, (b) Modified model (Eq. (4.25)) with lab scale data, (c) Modified model (Eq. (4.25)) with pilot scale data.

As illustrated in Figure 5.31a and 5.31b for lab scale prediction, it was noticed that a modified model provided slightly higher predictive accuracy with satisfactory agreement at ±32% of error. However, it seemed that this increasing model accuracy was insignificant since the original model (Eq. (4.23)) offered relatively high in the predictability at ±35% of error range. The fairly well consistence in time comparison of pilot scale data was obtained satisfactorily, as shown in Figure 5.31c.

As discussed in Chapter 4, the characteristics of C_{new} and E_{μ}/R were dependent on the ash compositions and possibly they were correlated mathematically with the variable terms, proposed in this work, which represent the fuel inorganic chemistry well known as Alkali Index (AI) and Base-to-Acid ratio ($R_{b/a}$) [112]. Early mentioned, they were defined as;

$$AI = \frac{kg(K_2O + Na_2O)}{GJ} \tag{2.6}$$

$$R_{b/a} = \frac{\%(Fe_2O_3 + CaO + MgO + K_2O + Na_2O)}{\%(SiO_2 + TiO_2 + Al_2O_3)} \tag{2.7}$$

The alkali index expresses the specific quantity of total alkali oxides in fuel (per unit mass of fuel) divided by heating value in GJ unit. HHV was selected in this study. Base-to-Acid ratio is defined as the ratio of basic oxide to acid oxide where the label for each compound makes reference to its weight concentration in the ash. Both indexes can be estimated by the fundamental fuel data of intensive laboratory characterization.

The MLR analysis further correlated C_{new} and E_{μ}/R of an individual biomass in Table 5.9 with AI and $R_{b/a}$ calculated from the corresponding ash data in Table 5.2 and 5.3. It provided the empirical correlations of AI and $R_{b/a}$ in Equation 5.1 and 5.2, respectively, and their prediction results with satisfactory agreement were illustrated in Figure 5.32.

$$C_{new} = 2.14x10^{-10} * (AI^{-1.55}) * (R_{b/a}^{-13.32}) \qquad (5.1)$$

$$E_{\mu}/R = 18543.47 * (AI^{-0.3}) * (R_{b/a}^{0.15}) \qquad (5.2)$$

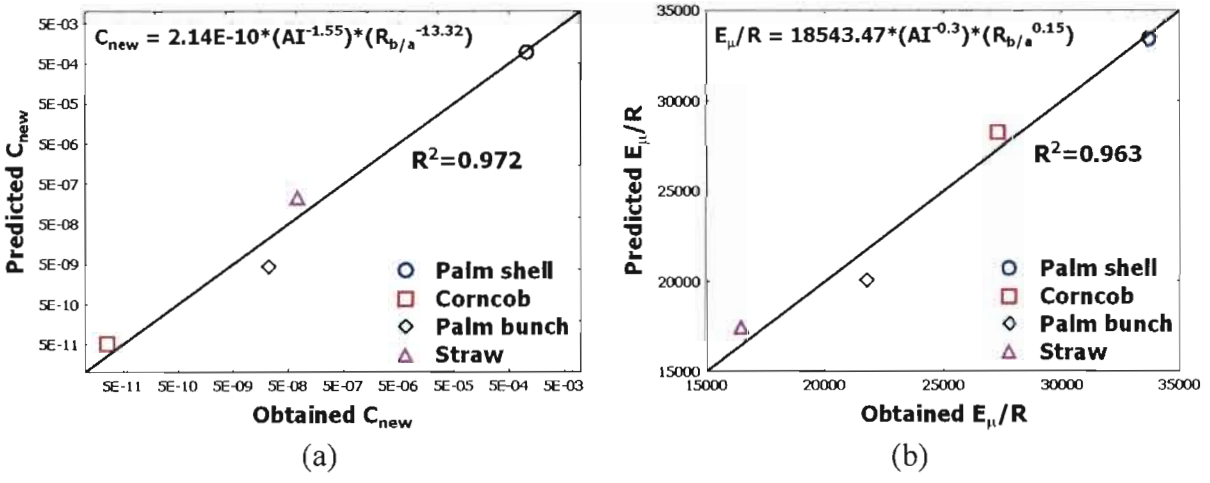

(a) (b)

Figure 5.32 Regression summaries of (a) C_{new} and (b) E_{μ}/R

When Equation 4.25, 5.1 and 5.2 at A=1 were employed to revise the verification of lab scale and pilot scale data, the obtained results were then reported in Figure 5.33 with fairly well agreement. This may be due to the using of a small number of biomass to perform the regression analysis in order to get C_{new} and E_{μ} equations, and their inaccuracy was included in the prediction.

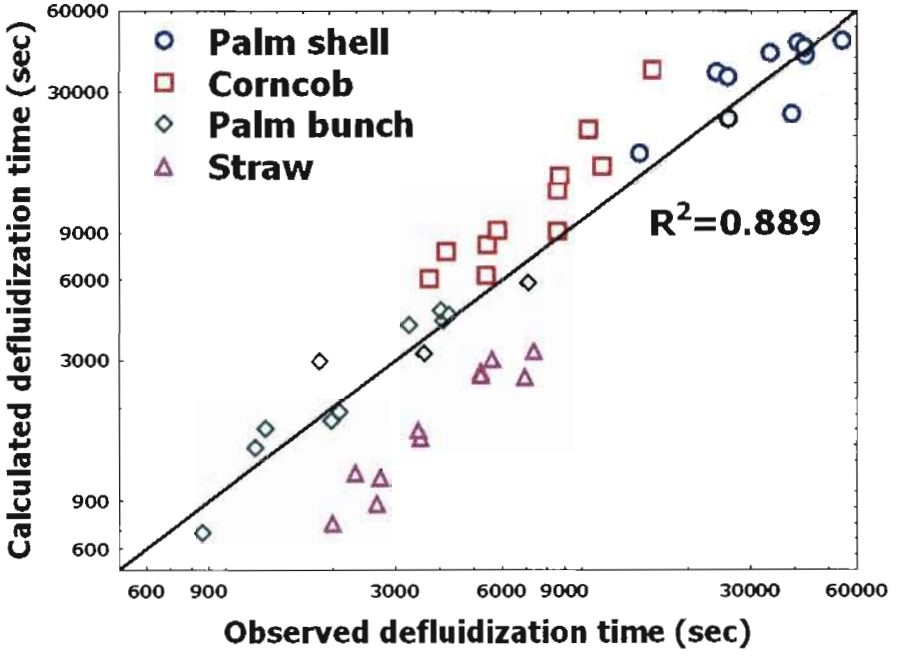

(a)

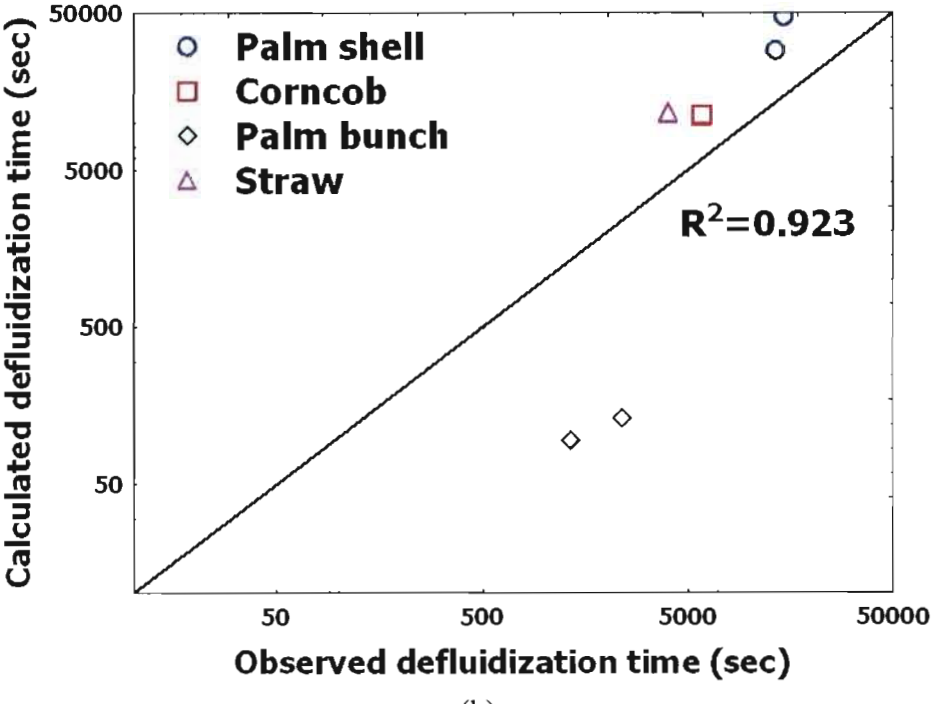

(b)

Figure 5.33 Revised t_{def} predictions to (a) lab scale data and (b) pilot scale data by Equation 4.25, 5.1 and 5.2.

In summary, the simple models in both newly proposed and modified from a previously published model were intentionally applied to describe the defluidization behaviors by bed agglomeration as dependence of the significant bed operating variable and biomass ash characteristics. The correlations newly set up by the dimensionless analysis and semi-empirical approach showed fairly well to good satisfactory agreement to the present experimental results. More experiments with the various types of biomass and operating conditions of FBC are therefore needed to improve these correlations.